Design of a validation campaign for electromagnetic modelling tools

Francesco Rigobello

Contents

Introduction

The present thesis is aimed to document the results achieved during a four months internship period at the European Space Agengy, ESTEC - Antenna Section. The work had the intent to study and design a validation campaign for electromagnetic modelling tools.

Within the development of mathematical models for the characterization of a problem from an electromagnetic point of view, a fundamental step consists in testing the accuracy of the model under discussion. The validation procedure allows to achieve an estimate of the degree of accuracy of the model with respect to the actual physical and electromagnetic configuration represented, by comparing the results of a simulation against a known reference. As we are dealing with antennas, typically the reference is obtained by measurements performed in an anechoic chamber. For this purpose, we have to prepare testing configurations, to be measured, that result to be critical towards the underlying computational technique, in terms of errors introduced by the simulation tool in reproducing the configuration under analysis.

In particular, this work will focus on antennas for space applications and the results will be applied as guidelines in the validation campaign of computational electromagnetics (CEM) modelling of a satellite mock-up.

The satellite payload is generally equipped with several antennas, assigned to different communication subsets, that are to be tested separately in order to verify their correct working. The spatial distribution of the radiated field is affected by other antennas and by the satellite body that behave as scattering elements and form together a complex structure from an electromagnetic point of view.

When modelling a structure as the one described, neglecting relevant details might compromise the simulation accuracy. Therefore, a particular attention must be paid in describing the whole environment surrounding the antennas, including the satellite body.

Accordingly, the validation results to be a crucial phase, and several configurations of antenna installations on the mock-up have to be taken into account in order to stress appropiately the simulation tool.

The goal of this work consists in developing a set of procedures that allow the engineer involved in a validation campaign to be able to decide among various feasible configurations those that can result critical for a simulation based on a given computational technique, and therefore to prepare a suitable measurement setup.

In order to do this, we will study how to compute indicators of the goodness of fit betweeen the simulation and the reference, and we will refer to these indicators as metrics. Some of these metrics will describe the trend of the slowly varying components of the field, others the rapidly changing features, and still others will give an indication of the global behavior of the field. Depending on the configuration being examined, some metrics might result more useful with respect to others, and a section of this work will propose a methodology to investigate in this direction.

Once this study has been completed, we will proceed with the configuration phase, in which several antennas are prepared for being installed on the satellite mock-up, see Fig.(1), in order to collect measurement references and move to the actual validation of tool simulated models.

Figure 1: FUSS satellite

Chapter 1

CEM techniques

General

Computational electromagnetics is the process of modeling the interaction of electromagnetic fields with physical objects and the environment.

Despite all CEM codes having their basis in Maxwell's equations, their accuracy and convergence depends on how the physics equations are cast (integral or differential form), inherent modeling limitations and approximations and which numerical solver approach is used.

The choice of the modelling technique that best suits the resolution of a given problem is a fundamental task, and is influenced by several criteria and requirements:

- The complexity of the problem to be solved.

- The modeling accuracy desired versus inherent limitations of the physics, modeling technique or software code.

- The existence of open or closed geometries and boundaries.

We present an overview on some CEM techniques used for antenna modeling and simulation, analysing their strengths and limitations in solving EM problems.

1.1 Physical Optics

Physical Optics (PO) is a technique that combines the use of Green's functions to calculate fields radiated by a given distribution of currents and then uses boundary conditions to determine the currents induced on objects due to incident fields. The effects due to mounting structures is computed by inducing currents on them and adding their radiation to the antenna pattern.

The radiated field can be found from distribution of the electric and magnetic currents by the use of Green's functions that contain source and field coordinates:

$$\mathbf{E}(\mathbf{r}) = \int \mathbf{G}_{EJ}(\mathbf{r},\mathbf{r'}) \cdot \mathbf{J}(\mathbf{r'}) \, dV' + \int \mathbf{G}_{EM}(\mathbf{r},\mathbf{r'}) \cdot \mathbf{M}(\mathbf{r'}) \, dV' \qquad (1.1)$$

$$\mathbf{H}(\mathbf{r}) = \int \mathbf{G}_{HJ}(\mathbf{r},\mathbf{r'}) \cdot \mathbf{J}(\mathbf{r'}) \, dV' + \int \mathbf{G}_{HM}(\mathbf{r},\mathbf{r'}) \cdot \mathbf{M}(\mathbf{r'}) \, dV' \qquad (1.2)$$

Physical optics starts with a given current distribution that radiates, or the measured pattern of an antenna. When an object is placed in the radiated field, the method calculates induced current on the object to satisfy the internal field condition.
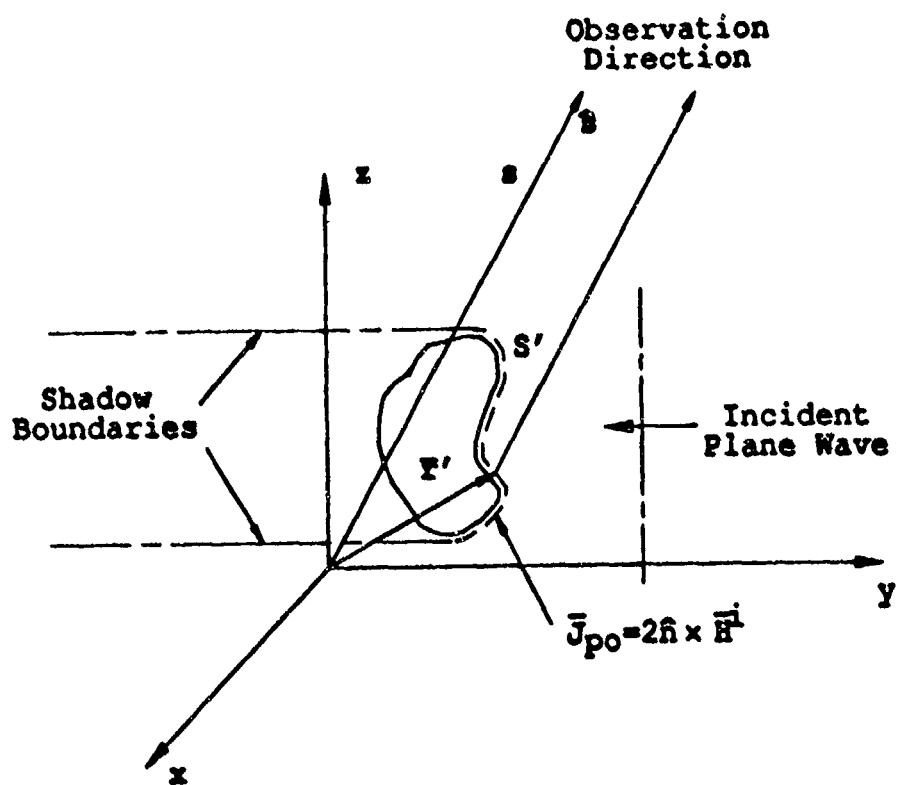
Figure 1.1: PO induced currents on a scatterer

Referring to Figure (1.1), consider a field incident on an PEC body, where the illuminated and shadowed regions are determinated using ray optics, and the incident magnetic field $\mathbf{H}_{incident}$ on the surface is approximated by the geometrical optics (GO) incident field; the induced surface current density is given by:

$$\mathbf{J}_S = \hat{\mathbf{n}} \times (\mathbf{H}_{incident} + \mathbf{H}_{reflected}) \tag{1.3}$$

$$\mathbf{H}_{incident} = \mathbf{H}_{reflected}$$

$$\mathbf{J}_S = \begin{cases} 2\hat{\mathbf{n}} \times \mathbf{H}_{incident} & \text{in lit regions} \\ 0 & \text{in shadow regions} \end{cases} \tag{1.4}$$

The far field is found using the far zone radiation integral which is defined by:

$$\mathbf{E}^s(s) = \frac{jkZ_0}{4\pi} \frac{e^{-jks}}{s} \int_{S'} \mathbf{J}(\mathbf{r'}) e^{jk\hat{s}\cdot\mathbf{r'}} dS' \tag{1.5}$$

Substituting the PO approximation to the surface current gives:

$$\mathbf{E}^s(s) = \frac{jkZ_0}{4\pi} \frac{e^{-jks}}{s} \int_{S'} 2\hat{n} \times \mathbf{H}(\mathbf{r'}) e^{jk\hat{s}\cdot\mathbf{r'}} dS' \tag{1.6}$$

where S' is the illuminated region on the scattering surface and s, $\hat{s}$ and $\mathbf{r'}$ are defined in Figure (1.1).

1.2 Method of Moments

The Method of Moments is a numerical technique based on the method of weighted residuals. It is appropriate in analysing electrically small to moderately sized unbounded radiation problems and excels in analysing PEC configurations and homogeneous dielectrics. This technique is based on integral equations, and electromagnetic fields are computed from wire mesh currents and patch surface current densities.

1.2.1 Steps of the method

Equations to be solved are linear operator equations in terms of the unknowns (the sources), which have the form

$$L(f) = g \tag{1.7}$$

where L is a linear operator, g is the source or excitation and f is the field or response, which is the unknown function to be determined.

The unknown quantity f is approximated by a finite series:

$$f \approx \sum_{n=1}^{N} \alpha_n f_n \tag{1.8}$$

where f_n are linear independent known functions, referred to as expansion functions and α_n are unknown coefficients yet to be determined. In general, expansion functions should be selected such that the solution is well approximated by a relative small number of functions.

Substituting Equation (1.8) in (1.7):

$$L\left(\sum_{n=1}^{N} \alpha_n f_n\right) \approx g \tag{1.9}$$

and exploiting the linearity of the operator, we obtain Equation (1.10).

$$\sum_{n=1}^{N} \alpha_n L(f_n) \approx g \tag{1.10}$$

Such an equation can not be satisfied exactly at all points, since the series has a finite number of terms, so a set of unknown coefficients (α_n) is required to satisfy it in a sense. To describe the degree of accuracy to which the left and the right side of Equation (1.10) match, a known weighting function, w_m is introduced. The function w_m is used to multiply both sides of Equation (1.10) and the results are integrated over a spatial region of interest.

$$\sum_{n=1}^{N} \alpha_n \langle w_m, L\left(f_n\right) \rangle = \langle w_m, g \rangle \tag{1.11}$$

This integration is a special case of an inner product of two functions, f and g, which is denoted by $\langle f, g \rangle$. To provide an efficient solution, the weighting functions should provide a reliable measure of discrepancy between the two sides of Equation (1.10).

$$\sum_{n=1}^{N} \alpha_n \langle w_m, L\left(f_n\right) \rangle = \langle w_m, g \rangle \quad m = 1, ..., N \tag{1.12}$$

Equation (1.12) represents a system of N ordinary linear equations in N unknowns. The solution of the matrix equation determines the coefficients of current expansion.

The expansion and weighting functions are chosen arbitrarily, according to consideration based on experience and computational requirements of the code that uses the MoM.

Both expansion and testing functions can be divided in two categories.

1.2.2   Subdomain functions

The domain, where the unknown function (f) is defined, is divided into a number of small subdomains. The basis functions are chosen as very simple functions, and each one is defined only on one subdomain.

Below some subdomain approximations are briefly presented.

Impulse functions

The simplest approach to subdomain approximation is to use Dirac's delta functions. Impulses are usually used as weighting functions, rather than for expansion.

$$w_m = \delta_m(P_m) \tag{1.13}$$

Thus, the inner product yields:

$$\langle w_m, g \rangle = g(P_m), \tag{1.14}$$

according to the integration of the product of the impulse with a function.

In this way, Equation (1.11) can be interpreted as matching the values of the left and right sides at the point P_m. Consequentially, Equation (1.12) requires Equation (1.10) to be simultaneously satisfied at N discrete matching points, P_m, $m = 1, ..., N$. This method simplifies the calculation of the matrix elements, as it avoids any integral computation. On the other hand, there is no guarantee about the behaviour of the error, except for matching points.

Pulse functions

Pulse function yield a staircase approximation of f. A pulse is defined as a piecewise-constant function:

$$f_n = \begin{cases} 1 & \text{in subdomain } n \\ 0 & \text{elsewhere} \end{cases}$$

Another consideration to take into account in the approximation by expansion functions concerns the geometry of the problem analysed: the subdomains may not match exactly the shape of the domain.

1.2.3 Entire-domain functions

Testing and expansion functions are now defined on the entire domain of interest, so that they are non-zero on the whole domain. In the numerical implementation of the entire-domain approximations, a complicated evaluation of matrix elements is often encountered, requiring high-precision computations.

1.2.4 Formulation of integral equations

To formulate the integral equations, a relation between the field and the field sources is required. All moment method solutions are found from the solution of integral equations over boundary conditions. The boundary conditions can be either the tangential electric field (EFIE) or magnetic field (MFIE) conditions

Boundary condition

Firstly, Equations (1.15) and (1.16) are imposed to provide a boundary condition for the electric or magnetic field.

$$\mathbf{n}\times\mathbf{E}_1-\mathbf{n}\times\mathbf{E}_2 = 0, \ \mathbf{n}\times\mathbf{H}_1-\mathbf{n}\times\mathbf{H}_2 = \mathbf{J}_s, \ \mathbf{n}\cdot\mathbf{D}_1-\mathbf{n}\cdot\mathbf{D}_2 = \rho_s, \ \mathbf{n}\cdot\mathbf{B}_1-\mathbf{n}\cdot\mathbf{B}_2 = 0 \tag{1.15}$$

If medium 2 is a PEC, Equation (1.15) reduces to:

$$\mathbf{n} \times \mathbf{E}_1 = 0, \ \mathbf{n} \times \mathbf{H}_1 = \mathbf{J}_s, \ \mathbf{n} \cdot \mathbf{D}_1 = \rho_s \mathbf{n} \cdot \mathbf{B}_1 = 0 \tag{1.16}$$

Potentials expression

Secondly, Equation (1.17) or (1.18) is used to express the electric and magnetic fields in terms of the electric scalar-potential (V) and the magnetic vector-potential ($\mathbf{A}$).

$$\mathbf{E} = -j\omega\mathbf{A} - \nabla V, \ \ \mathbf{B} = \nabla \times \mathbf{A} \tag{1.17}$$

$$\mathbf{E} = -j\omega\left(\mathbf{A} + \frac{1}{k^2}\nabla\left(\nabla \cdot \mathbf{A}\right)\right) \tag{1.18}$$

Field sources relations

Thirdly, for a linear homogeneous lossless medium, Equation (1.19) relates the potentials to the field sources leading to the expression of integral equation for the unknown field sources.

$$\mathbf{A}(\mathbf{r}) = \mu\int_{\nu'}\mathbf{J}(\mathbf{r'})g(\mathbf{r},\mathbf{r'})d\nu', \ \ V(\mathbf{r}) = \frac{1}{\varepsilon}\int_{\nu'}\rho(\mathbf{r'})g(\mathbf{r},\mathbf{r'})d\nu' \tag{1.19}$$

If considering surface sources Equation (1.19) is to be modified:

$$\mathbf{A}(\mathbf{r}) = \mu\int_{S'}\mathbf{J}_s(\mathbf{r'})g(\mathbf{r},\mathbf{r'})dS', \ \ V(\mathbf{r}) = \frac{1}{\varepsilon}\int_{S'}\rho_s(\mathbf{r'})g(\mathbf{r},\mathbf{r'})dS' \tag{1.20}$$

where $\mathbf{J}_s$ and ρ_s in Equation (1.20) are respectively the density of the surface currents and the density of charges, and S' is the source surface.

If considering filamental sources Equation (1.19) take the form represented in Equation (1.21).

$$\mathbf{A}(\mathbf{r}) = \mu\int_{L'}\mathbf{u}(\mathbf{r'})I(\mathbf{r'})g(\mathbf{r},\mathbf{r'})dl', \ \ V(\mathbf{r}) = \frac{1}{\varepsilon}\int_{L'}\rho_l(\mathbf{r'})g(\mathbf{r},\mathbf{r'})dl' \tag{1.21}$$

where $\mathbf{u}$ is the unit vector tangential to the line.

1.2.5 MoM applied to Antennas

The Method of Moments is the most widely used CEM method for antenna engineering, as it is applicable to many antenna types. The MoM can handle antennas whose dimensions are very small, a fraction of the wavelength, up to about one thousand wavelengths for wire antennas. According to this method, the radiating/scattering structure is replaced by equivalent currents, usually surface currents. The analysis has to take into account also the environment where the antenna is located, like a mounting mast or a stratified ground. Hence, the applicability of MoM depends, and is limited, from both the complexity of the antenna, which requires a precise modelling

of various physical antenna parts, and the overall antenna dimensions, since to guarantee an efficient radiation the minimum size has to be in the order of magnitude of 1/10 of the operating frequency. Well-written MoM codes, however, can analyse structures whose dimensions are many orders of magnitude smaller.

1.3 Uniform Theory of Diffraction

Geometrical theory of diffraction and its extension Uniform theory of diffraction are high-frequency ray tracing techniques.

Geometrical optics, the most widely used theory of light propagation, can be used to determine the fields as the wavelength of an electromagnetic excitation approaches zero, but fails to account for certain phenomena called diffraction. GTD and UTD methods add diffracted rays to GO rays to obtain an improved estimate of the exact field solution. Diffracted rays are produced by incident rays which hit edges, corners, or vertices of boundary surfaces, or which graze such surfaces.

Diffraction is a local phenomenon at high frequencies, therefore the behaviour of the diffracted wave at edges, corners, and surfaces can be determined from an asymptotic form of the exact solution for simpler canonical problems.

These techniques are accurate when the dimensions of the analysed objects are electrically large, relatively to the wavelength of the field.

1.3.1 Boundaries

Let us refer to the situation depicted in Figure (1.2), where a plane perpendicular to the edge at point of diffraction Q_E is shown.

According to Keller's generalized Fermat's principle, the ray incident on the edge Q_E produces edge diffracted rays ed and surface diffracted rays sr. ES is the boundary between the edge diffracted rays and the surface diffracted rays, and it is tangent to the surface at Q_E. SB is the shadow boundary of the incident field and RV is the reflection boundary of the reflected field. Since the behaviour of the ray optics field is different in the two regions separated by a boundary, there is a transition region adjacent to each boundary within which there is a rapid variation of the field between the two regions.

The total electric field may be represented as:

$$\mathbf{E} = \mathbf{E}^i u^i + \mathbf{E}^r u^r + \mathbf{E}^d \tag{1.22}$$

Where u^i and u^r are unit step functions, that highlight the discontinuity in the incident and reflected fields at the shadow and reflection boundaries.

The correct high-frequency field must be continuous at the shadow and reflection boundaries, therefore the diffracted field presented in Equation (1.22) must provide the correct transition between the illuminated regions and the regions shadowed by the edge, as it penetrates the latter, which according to GO, has a zero field to account for the nonvanishing fields known to exist there.
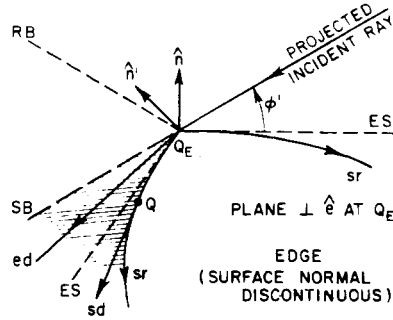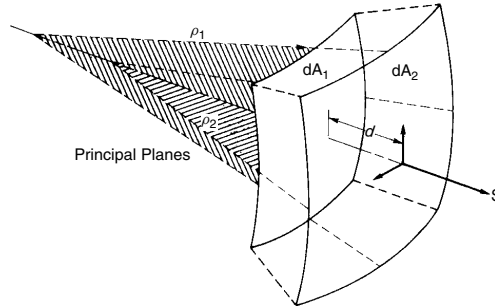
12

Figure 1.2: Shadow and reflection boundaries at Q_E

Figure 1.3: Astigmatic tube of rays

1.3.2 The Geometrical Optics field

The incident and reflected fields are expanded in Luneberg-Kline series:

$$\mathbf{E} \sim \exp(-jk\psi) \sum_{m=0}^{\infty} \frac{\mathbf{E}_m}{(jw)^m} \tag{1.23}$$

Substituting Equation (1.23) into the vector wave equation for the electric field and integrating the resulting transport equation for $m=0$, we obtain

$$\mathbf{E}(s) \sim \exp\left[-jk\psi(0)\right]\mathbf{E}_0(s) = \mathbf{E}_0(0)\exp\left[-jk\psi(0)\right]\sqrt{\frac{\rho_1\rho_2}{(\rho_1 + s)(\rho_2 + s)}}\exp\left(-jks\right) \tag{1.24}$$

that we recognize as the geometrical-optics field.

When $s = -\rho_1$ or $-\rho_2$, Equation (1.24) becomes infinite and consequently the approximation is no longer valid. Passage through a caustic causes an extra phase shift to the ray. While passing through either ρ_1 or ρ_2 the denominator factor in the square root of equation (1.24) produces a 180° sign change. When tracing a ray moving through a caustic in the

13

direction of propagation, the field is multiplied by $(e^{j\pi/2})$, and by $(e^{-j\pi/2})$ for a ray traced in the opposite direction.

Maxwell's equation $\nabla \times \mathbf{E} = -i\omega\mu\mathbf{H}$ is employed to find the leading term in the asymptotic approximation of the magnetic field, that is:

$$\mathbf{H} \sim Y_c \hat{s} \times \mathbf{E} \tag{1.25}$$

where $Y_c = \sqrt{\varepsilon/\mu}$ and $\hat{s}$ is a unit vector in the direction of the path. From $\nabla \cdot \mathbf{E} = 0$

$$\hat{s} \cdot \mathbf{E}_0 = 0 \tag{1.26}$$

Consider a high-frequency electromagnetic wave incident on a smooth curved perfectly conducting surface S, the geometrical optics electric reflected field has the form given in (1.24).

The boundary condition on perfectly conducting surface for the total electric field on S leads to:

$$\mathbf{E}_0^r(0) \exp\left[-jk\psi^r(0)\right] = \mathbf{E}^i(Q_R) \cdot \bar{R} = \mathbf{E}^i(Q_R) \cdot \left[\hat{e}_\parallel^i \hat{e}_\parallel^r - \hat{e}_\perp \hat{e}_\perp\right] \tag{1.27}$$

where $\bar{R}$ is the dyadic reflection coefficient and $E^i(Q_R)$ is the electric field incident at the reference point Q_R.

Combining Equations (1.24) and (1.27) one obtains:

$$\mathbf{E}^r(s) = \mathbf{E}^i(Q_R) \cdot \bar{R} \sqrt{\frac{\rho_1^r \rho_2^r}{(\rho_1^r + s)(\rho_2^r + s)}} \exp(-jks) \tag{1.28}$$

in which ρ_1^r and ρ_2^r are the principal radii of curvature of the reflected wavefront at the point of reflection.

1.3.3   The Edge diffracted field

Consider a smooth surface S which has a curved edge formed by a discontinuity in its normal vector.

Equation (1.24) can be arranged in order to show that it is also the leading term in the asymptotic approximation of the diffracted field.

Using the method of stationary phase, see Section (1.3.4), to evaluate the integral representation of the edge diffracted field over its wavefront gives

$$\mathbf{E}^d(s) \sim \mathbf{E}^d(0') \sqrt{\frac{\rho\rho'}{(\rho + s)(\rho' + s)}} \exp(-jks) \tag{1.29}$$

Since the diffracted field is proportional to the field incident at Q_E,

$$\lim_{\rho' \to 0} \mathbf{E}^d \left(0'\right) \sqrt{\rho'} = \mathbf{E}^i \left(Q_E\right) \cdot \bar{D} \tag{1.30}$$

where $\bar{D}$ is the dyadic edge diffraction coefficient. The edge diffracted field becomes, assuming that E^i is not rapidly varying at Q_E except for its phase variation,

$$\mathbf{E}^d(s) \sim \mathbf{E}^i \cdot \bar{D} \sqrt{\frac{\rho}{s\left(\rho + s\right)}} \exp\left(-jks\right) \tag{1.31}$$

where ρ is the distance between the caustic at the edge and the second caustic of the diffracted ray.

Equation (1.32) states an important relationship

$$\frac{1}{\rho} = \frac{1}{\rho_e^i} + \frac{1}{f} = \frac{1}{\rho_e^i} - \frac{\hat{n}_e \cdot \left(\hat{s}' - \hat{s}\right)}{a \sin^2 \beta_0} \tag{1.32}$$

where ρ_e^i is the radius of curvature of the incident wavefront at Q_E taken in the plane containing the incident ray and $\hat{e}$ the unit vector tangent to the edge at Q_E, $\hat{n}_e$ is the associated normal vector to the edge directed away from the center of curvature, $a > 0$ is the radius of curvature of the edge at Q_E, and β_0 is the angle between the incident ray and the tangent to the edge. The unit vectors $\hat{s}$ and $\hat{s}'$ are in the directions of incidence and diffraction respectively.

Equation (1.31) is not valid at the edge, since the high-frequency diffracted field has a caustic there, thus a procedure similar to that used to find the reflection coefficient can not be used.

A necessary condition that can help in finding the solution is represented by the matching of the phase functions at the edge

$$\psi_i(Q_E) = \psi_r(Q_E) = \psi_d(Q_E)$$

That leads to obtain the Equation (1.27)

$$\hat{e} \cdot \hat{s}' = \hat{e} \cdot \hat{s}^r = \hat{e} \cdot \hat{s} \tag{1.33}$$

That allows to formulate *Keller's law of edge diffraction*:

The angle of diffraction β_d is equal to the angle of incidence β_0, so that the diffracted rays emanating from Q_E form a cone whose half-angle is β_0 and whose axis is the tangent to the edge. The incident ray and the ray reflected from the surface at Q_E also lie on the cone of the diffracted rays.

The form of the dyadic diffraction coefficient can be simplified if the proper ray-fixed coordinate is chosen.

Referring to Figure (1.4), the plane of incidence contains the incident ray and the unit vector $\hat{e}$ tangent to the edge of the point of incidence Q_E. The
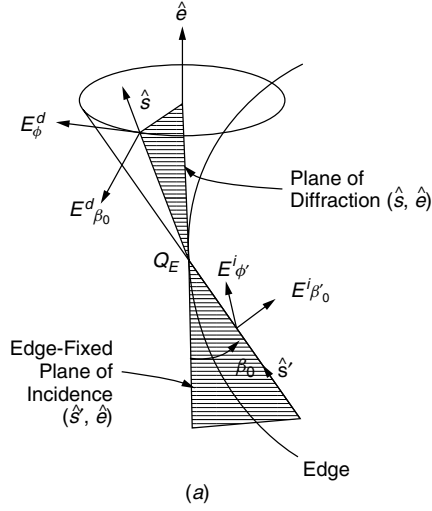
Figure 1.4

plane of diffraction contains the diffracted ray and $\hat{e}$. The unit vectors $\hat{\phi}'$ and $\hat{\phi}$ are perpendicular to the plane of incidence and the plane of diffraction respectively. The unit vectors $\hat{s}'$ and $\hat{s}$ are in the direction of incidence and in direction of diffraction respectively. The unit vectors $\hat{\beta}'_0$ and $\hat{\beta}_0$ are parallel to the edge-fixed plane of incidence and the plane of diffraction, respectively and

$$\hat{\beta}'_0 = \hat{s}' \times \hat{\phi}' \tag{1.34a}$$

$$\hat{\beta}_0 = \hat{s} \times \hat{\phi} \tag{1.34b}$$

Accordingly, a spherical coordinate system is introduced for both the diffracted ray $(s, \pi - \beta_0, \phi)$ and the incident ray (s', β_0, ϕ'), except that the incident radial unit vector points toward the origin Q_E.

The z components of the electric and magnetic fields in correspondence of this surface with an edge are given by

$$E_z = E^i_z + E^r_z + E^d_z \tag{1.35}$$

$$H_z = H^i_z + H^r_z + h^d_z \tag{1.36}$$

that satisfy

$$\left(\nabla^2 + k^2\right) \begin{Bmatrix} E_z \\ H_z \end{Bmatrix} = 0 \tag{1.37}$$

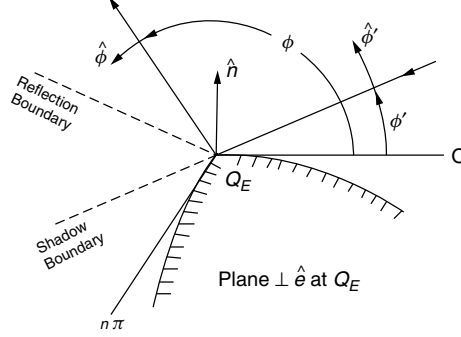and are subject to the soft or hard boundary conditions:

Figure 1.5

$$E_z = 0 \tag{1.38}$$

or

$$\frac{\partial H_z}{\partial n} = 0 \tag{1.39}$$

and to the radiation condition at infinity.

The high-frequency solution for the z components of the diffracted field may be put in the form

$$\left.\begin{array}{c} E_z^d \\ H_z^d \end{array}\right\} \sim \left.\begin{array}{cc} E_z^i & D_s \\ H_z^i & D_h \end{array}\right\} \sqrt{\frac{\rho}{s(\rho + s)}} \exp(-jks) \tag{1.40}$$

and from

$$E_z^i = E_{\beta_0'}^i \ \sin \beta_0 \tag{1.41}$$

$$H_z^i = Y_c \ E_{\phi'}^i \ \sin \beta_0 \tag{1.42}$$

it follows

$$\left.\begin{array}{c} E_{\beta_0}^d \\ H_\phi^d \end{array}\right\} = - \left.\begin{array}{cc} E_{\beta_0'}^i & D_s \\ E_{\phi'}^i & D_h \end{array}\right\} \sqrt{\frac{\rho}{s(\rho + s)}} \exp(-jks) \tag{1.43}$$

In conclusion, the dyadic diffraction coefficient for an ordinary edge in a perfectly conducting surface can be expressed as the sum of two dyads to first order

$$\bar{D} = -\hat{\beta}_0' \hat{\beta}_0 D_s - \hat{\phi}' \hat{\phi} D_h \tag{1.44}$$

17

1.3.4 Method of stationary phase

The stationary phase method is a widely used method for asymptotically evaluating a class of integrals of the form:

$$I(x) = \int_a^b F(x)e^{ik\phi(x)} \tag{1.45}$$

where $\phi(x)$ is a rapidly-varying function of x over most of the range of integration, and $F(x)$ is slowly-varying.

Rapid oscillations of the exponential term mean that I is approximately zero over those regions of the integrand: the only significant non-zero contributions to the integral occur in regions of the integration range where $d\phi/dx = 0$, i.e. at points of stationary phase.

Points of stationary phase are labeled x_s and defined by

$$\phi'(x_s) = 0 \tag{1.46}$$

Since $F(x)$ is assumed to be slowly-varying, $F(x) \approx F(x_s)$ in the neighbourhood of the stationary phase points; hence this term can be pulled outside the integral.

Expanding $\phi(x)$ in a Taylor series near the point x_s and keeping only the first two non-zero terms, one obtains

$$\phi(x) \approx \phi(x_s) + \frac{1}{2}\phi''(x_s)(x - x_s)^2 \tag{1.47}$$

Substituting this into the integral gives

$$I(k) \sim F(x_s)\sqrt{\frac{2\pi}{k|\phi''(x_s)|}}e^{j[k\phi(x_s)+\frac{\pi}{4}sgn(\phi''(x_s))]} \tag{1.48}$$

$$+\frac{1}{k}\frac{F(b)}{\phi'(b)}e^{j[k\phi(b)-\frac{\pi}{2}]} - \frac{1}{k}\frac{F(a)}{\phi'(a)}e^{j[k\phi(a)-\frac{\pi}{2}]} \tag{1.49}$$

Chapter 2

CEM modelling validation

2.1   General

Computational electromagnetics (CEM) techniques and codes provide solutions to a wide variety of electromagnetic applications, such as electromagnetic compatibility (EMC), radar cross section (RCS), signal integrity (SI) and antennas. However, many critical issues may appear during their implementation, and a fundamental task consists in determining whether the results are accurate or not.

The validation procedure allows to achieve an index of the degree of accuracy of the model with respect to the actual physical and electromagnetic configuration represented.

In the flowchart represented in Figure (2.1) we highlight the steps followed by the procedure presented in this work.

2.2   Levels of model validation

The levels involved in a complete model validation are three:

- Mathematical level: Computational technique level

- Implementation level: Individual software code implementation validation

- **Model level: Specific model validation**

2.2.1   Computational technique validation

When a new technique is developed, it must undergo extensive validation to determine its limitations, strengths, and accuracy. In order to achieve an exaustive experimental validation a wide range of models may be needed to
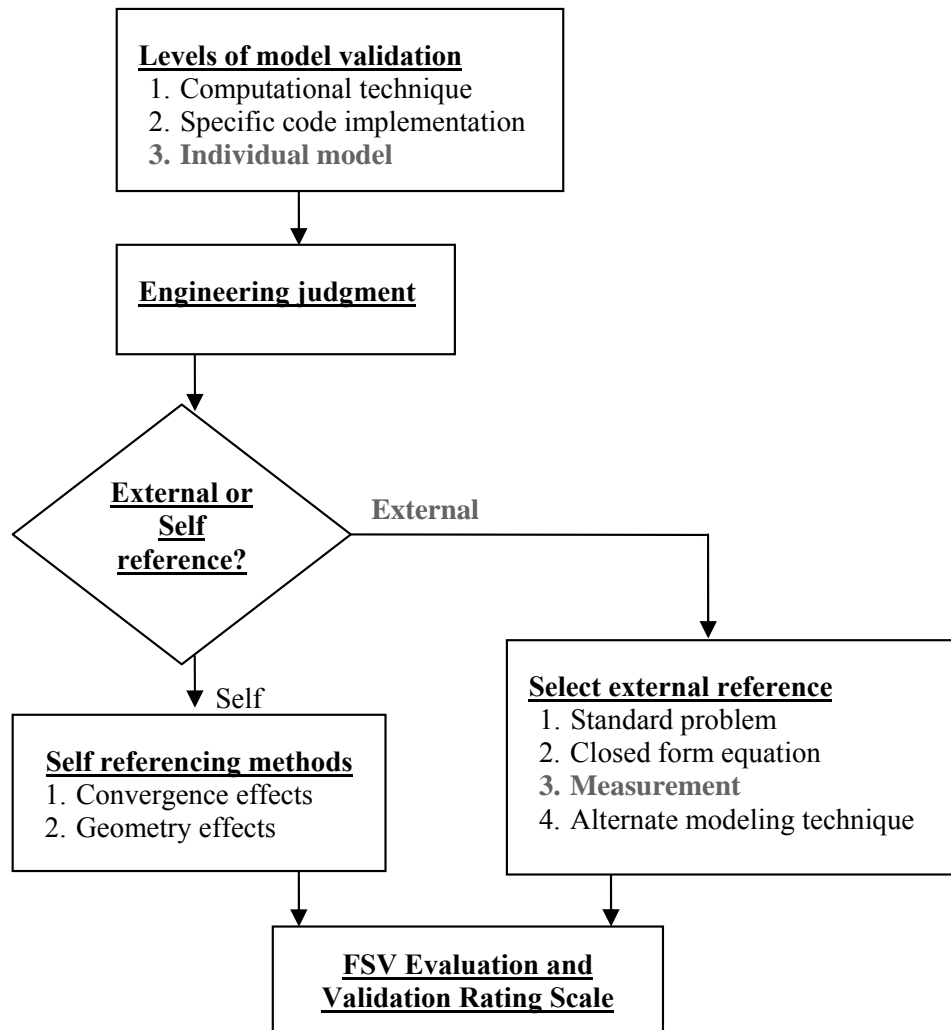
Figure 2.1: FSV Flowchart

fully bound the intended application. This step is usually unnecessary in most EM modeling problems.

2.2.2 Individual code implementation validation

This level is to ensure the veracity of the software implementation of the computational technique, and ensure the creation of correct results for the defined model.

2.2.3 Specific model validation

It is common to assume that software modelling tools provide an accurate solution to a given problem, so that validation procedure may skip the first two steps and focus on the third one. The solver might have received the wrong problem; in fact, the actual physical structure intended might have been represented with sources or other elements specified in an erroneous way.

2.3 External references

To perform a validation with an external reference, simulation results may be compared to different suitable references:

- Standard problems

- Closed-form equations

- **Measurements**

- Other modelling techniques

The selection of the reference is a critical task for the validation process.

2.3.1 Standard problem references

A number of standard validation problems involving printed circuit boards, antennas, and shielding have been proposed in order to provide assistance in evaluating various modeling tools against specific problems that are similar to the ones to be simulated. Solutions to these kind of problems are fully specified and can be used as the reference for model validation.

2.3.2 Closed-form equation references

Closed-form equations are generally specialized and may not represent the real-world problem of interest to the user. Therefore, closed-form equation references must be selected with care to ensure that they are appropiate for the situation.

2.3.3 Measurement references

Antenna and RCS measurements may be made with high precision, and can be used as references for validation as they provide very accurate results.

On the CEM modelling side, several issues have to be taken into account, in order to minimize measurement-related validation uncertainties:

- The measurement environment geometry must be accurately represented in the model

- Overall measurement accuracy must be understood

- Loading effects of measurement equipment must be included

The goal is to ensure that the measured problem geometry and the simulated one are identical in every aspect.

2.4 Feature Selective Validation

The Feature Selective Validation (FSV) method is a technique for the quantitative validation of computational electromagnetics (CEM) modelling. This procedure is used to determine whether the agreement between the validation reference and simulation results is acceptable.

FSV allows the comparison between two set of data to be quantified objectively, by decomposing the results into two component measures which are combined to provide a global goodness of fit measure:

- The Amplitude Difference Measure (ADM) compares the amplitudes and 'trends' of the two data sets

- The Feature Difference Measure (FDM) compares the rapidly changing features

- The Global Difference Measure (GDM) gives an overall single figure goodness-of-fit between the two data sets being compared and allows a simple decision to be made about the quality of comparison (numerical or converted to a natural language descriptor).

2.4.1 Validation Rating Scale

The Validation Rating Scale (VRS) establishes a benchmarking technique, allowing visual comparisons to be made between experimental and simulated data.

Validation of EM modeling methods, particularly against experimental results, often involves structurally complex data sets. Quantification made 'by eye', to determine how similar two traces appear, has obvious limitations

due to the subjectivity of this approach. Furthermore, there is no absolute scale to make the comparisons by. The VRS provides the confidence that is lacking in the old visual approach.

The VRS is a six-point scale requiring only a binary decision at each node, and therefore no subjectivity is left in the validation process. Qualitative, natural language descriptors have been allocated to this values: excellent, very good, good, fair, poor and very poor, reflecting a common comparative lexicon.

2.4.2 Method

Let two separate data sets be available for comparison, both sharing a common independent variable (x-axis values) and a common dependent variable (y-axis values). The two data sets may:

- Contain different numbers of data points

- Exist over different ranges of the common independent variable

- Have either coincident or noncoincident values of the common independent variable

The procedure to compute the ADM and the FDM, and consequentially the GDM consists of 14 steps:

- *Input data sets are proceeded to generate the working data sets.* In the end the two working data sets contain the same number of data points and have coincident values of the common independent variable.

- *Computation of the transformed data sets.* Fourier transform both working data sets.

- *Calculation of the "low" data sets.*

  - Avoid DC and very low frequency components, (by ignoring the first four points in the transformed data set)
  - Sum the intensities of the remaining data

$$S = \sum_{i=5}^{N} TWDS(i)$$

  - Determine the 40% location.

$$\sum_{i=5}^{i_{40\%}} TWDS(i) \geq 0.4 \times S$$

  where $i_{40\%}$ is the element containing the 40% location.

23

– Determine the 'break-point' location. The 40% location used by the FSV is the lowest of the two resulting numbers (from the two original data sets).

$$i_{bp} = i_{40\%} + 5$$

– Low-pass filter the transformed data.

Element number	Filter value
$i_{bp} - 3$	1.000
$i_{bp} - 2$	0.834
$i_{bp} - 1$	0.667
i_{bp}	0.500
$i_{bp} + 1$	0.334
$i_{bp} + 2$	0.167
$i_{bp} + 3$	0.000

Table 2.1: Filter definition

– Inverse Fourier transform on the filtered transformed data set. Label the returned vectors as $Lo_1(f)$ and $Lo_2(f)$.

• *Calculation of the "high" data sets.*

– *High-pass filter the transformed data.*

Element number	Filter value
$i_{bp} - 3$	0.000
$i_{bp} - 2$	0.167
$i_{bp} - 1$	0.334
i_{bp}	0.500
$i_{bp} + 1$	0.667
$i_{bp} + 2$	0.834
$i_{bp} + 3$	1.000

Table 2.2: Filter definition

– Inverse Fourier transform on the filtered transformed data set. Label the returned vectors as $Hi_1(f)$ and $Hi_2(f)$.

• *Calculate the ADM on a point-by-point basis.*

$$ADM(f) = \left| \frac{(|Lo_1(f)| - |Lo_2(f)|)}{\frac{1}{N} \sum_{i=1}^{N} (|Lo_1(f)| + |Lo_2(f)|)} \right|$$

- *Calculate the mean value of ADM.*

$$ADM = \frac{\sum\limits_{f_{min}}^{f_{max}} ADM(f)}{N} \tag{2.1}$$

- *Calculate the ADM confidence histogram.*

FSV value (quantitative)	FSV interpretation (qualitative)
Less than 0.1	Excellent
Between 0.1 and 0.2	Very good
Between 0.2 and 0.4	Good
Between 0.4 and 0.8	Fair
Between 0.8 and 1.6	Poor
Greater than 1.6	Very poor

Table 2.3: Confidence histogram

- *Calculate derivatives in preparation for the FDM calculation.*
    - The first derivatives of the $Lo(f)$ and $Hi(f)$ data sets.
    - The second derivatives of the $Hi(f)$ data sets.

The derivatives accentuate the high rate-of-change features in the original data.

The first derivatives are obtained using a central difference scheme as in Equation (2.2)

$$Lo'(f) = Lo(f + N_d) - Lo(f - N_d) \tag{2.2}$$

where $N_d = 2$

The second derivatives are obtained from the first derivatives using an approach as in Equation (2.3)

$$Hi''(f) = Hi'(f + N_d) - Hi'(f - N_d) \tag{2.3}$$

where $N_d = 3$

- *Calculate the point-by-point FDM.* The FDM is composed of three parts, as described by Equations (2.4), (2.5) and (2.6).

$$FDM_1(f) = \frac{|Lo'_1(f)| - |Lo'_2(f)|}{\frac{2}{N}\sum\limits_{i=1}^{N}\left(|Lo'_1(i)| + |Lo'_2(i)|\right)} \tag{2.4}$$

$$FDM_2(f) = \frac{|Hi_1'(f)| - |Hi_2'(f)|}{\frac{6}{N}\sum\limits_{i=1}^{N}(|Hi_1'(i)| + |Hi_2'(i)|)} \tag{2.5}$$

$$FDM_3(f) = \frac{|Hi_1''(f)| - |Hi_2''(f)|}{\frac{7.2}{N}\sum\limits_{i=1}^{N}(|Hi_1''(i)| + |Hi_2''(i)|)} \tag{2.6}$$

Equations (2.4), (2.5), (2.6) are combined resulting in Equation (2.7).

$$FDM(f) = 2\left(|FDM_1(f) + FDM_2(f) + FDM_3(f)|\right) \tag{2.7}$$

- *Calculate the single value of FDM.*

$$FDM = \frac{\sum\limits_{f_{min}}^{f_{max}} FDM(f)}{N} \tag{2.8}$$

- *Calculate the FDM confidence histogram.*

- *Obtain the point-by-point GDM value.*

  Assuming the ADM and FDM being largely independent:

$$GDM(f) = \sqrt{ADM(f)^2 + FDM(f)^2} \tag{2.9}$$

- *Calculate the overall GDM value and the GDM confidence histogram.*

- *Determine the equivalent visual scale values for ADM, FDM, and GDM.* The FSV values are scaled to a visual, six-point scale.

  The piece-wise approach is given in Table (2.4).

If X ≤ 0.1 Then V = 1 + 10X
If X > 0.1 and X ≤ 0.2 Then V = 2 + 10(X-0.099)
If X > 0.2 and X ≤ 0.4 Then V = 3 + 5(X-0.199)
If X > 0.4 and X ≤ 0.8 Then V = 4 + 2.5(X-0.399)
If X > 0.8 and X ≤ 1.6 Then V = 5 + 1.25(X-0.799)
If X > 1.6 Then V = 6

Table 2.4: Piecewise visual conversion

2.4.3 Grade and spread

An improvement of the FSV might be achieved by weighting the ADM and FDM in the GDM calculation according to:

- **Grade**: how concentrated the histogram bars are at one extreme or the other.

- **Spread**: how dispersed the histogram bars are around the mean value.

The *grade* gives a numerical indication of the quality of the comparison. It is given a numerical value by counting how many categories (starting from excellent) are required for the cumulative total of the histogram to exceed a given value.

The *spread* gives a numerical indication of the level of confidence that can be placed on this assessment. A numerical value is given to it by counting how many adjacent categories (starting from the largest) are required to cumulatively exceed a given value.

2.5 RF Error Metrics

An additional specialized set of metrics has been developed in [1] and can be used in order to evaluate the accuracy of a model with respect to a measurement reference.

The quantities introduced to describe the performances are:

- **Field relative residual:** a scalar quantity that measures the deviation of the perturbed (simulated) field from the reference one.

$$\varepsilon_M = \sqrt{\frac{\iint\limits_{S} \left| \tilde{E}(\theta,\phi) - E(\theta,\phi) \right|^2 dS}{\iint\limits_{S} |E(\theta,\phi)|^2 dS}} \qquad (2.10)$$

- **Pointwise normalized relative deviation:** a distributed quantity that measures the pointwise normalized relative deviation of the perturbed (simulated) field from the reference one.

$$rel_{DEV} = \sqrt{\frac{\left| \tilde{E}(\theta,\phi) - E(\theta,\phi) \right|^2}{\iint\limits_{S} |E(\theta,\phi)|^2 dS}} \qquad (2.11)$$

- **The Degree of Correlation:** a factor that gives an indicator of the degree of correlation between the simulated and the reference field.

$$DoC = \frac{\left| \iint\limits_{S} [\tilde{E}(\theta,\phi)][E(\theta,\phi)]^* \, dS \right|^2}{\iint\limits_{S} |E(\theta,\phi)|^2 dS \iint\limits_{S} |\tilde{E}(\theta,\phi)|^2 dS} \qquad (2.12)$$

where $E(\theta,\phi)$ and $\tilde{E}(\theta,\phi)$ are respectively the radiation pattern of reference field and perturbed (simulated) field and $dS = \sin\theta d\theta d\phi$ is the portion of the sphere under analysis.

This work introduces a methodology that tries to merge the two approaches presented in Chapter (2.5) and (2.6) by applying the latter RF metrics to 'low' and 'high' data sets as defined in the FSV. In particular, 'low' and 'high' components of the field relative residual, as computed in (2.13) and (2.14), will result of interest for this thesis purposes.

$$\varepsilon_{M_{LO}} = \sqrt{\frac{\iint\limits_{S} \left| \tilde{E}_{LO}(\theta,\phi) - E_{LO}(\theta,\phi) \right|^2 dS}{\iint\limits_{S} |E_{LO}(\theta,\phi)|^2 dS}} \tag{2.13}$$

$$\varepsilon_{M_{HI}} = \sqrt{\frac{\iint\limits_{S} \left| \tilde{E}_{HI}(\theta,\phi) - E_{HI}(\theta,\phi) \right|^2 dS}{\iint\limits_{S} |E_{HI}(\theta,\phi)|^2 dS}} \tag{2.14}$$

For clarity reasons, we will refer to *Field relative residual* computed on low frequencies, high frequencies and the whole spectrum as RRLF, RRHF and RR respectively. Furthermore, hereafter, ADM, FDM and GDM will be referred to as Metric Set 1 components, and RRLF, RRHF, RR as Metric Set 2.

The reason beside the decision of working with more than one set of metrics on the same data, is the aim to discover if a metric might give more useful information with respect to the others, for some radiation patterns under analysis.

A final resume of metrics used in this work is presented in Tab.(2.5) and (2.6).

Metric	Metric Set 1			Metric Set 2		
Acronym	ADM	FDM	GDM	RRLF	RRHF	RR

Table 2.5: Metric Sets

Metric	Pointwise Relative Deviation	Degree of Correlation
Acronym	RD	DoC

Table 2.6: RF Metrics

Chapter 3

Error Analysis

Introduction

A crucial task in the validation procedure is to decide whether an antenna measurement configuration, and therefore the related radiation pattern, can be useful or not in order to validate a model based on a definite CEM technique.

The goal of this work is to investigate if and when a radiation pattern can be more or less useful to validate an electromagnetic modelling tool that relies on a chosen technique. Metrics introduced in Chapter (2) are used as means to quantify the sensitivity of a pattern to different types of errors. Furthermore, we can use different sets of metrics to analyse the same cases and compare the results to see which one can provide more useful information.

First, we analytically study the numerical error related to PO, MoM and GTD/UTD modelling. Second, we select antenna patterns on which errors previously described are simulated. Last, we observe how patterns respond to errors. This is done and quantified by means of metrics that are linked to different spectral components of the field. We refer to intra-metric analysis when for a given type of error, we fix the metric and observe the response of different patterns. On the other hand, we refer to inter-metric analysis as we select the configuration and compare different metrics computed on it.

3.1 Numerical error

Below some hypothesis about numerical errors introduced by different modeling techniques are formulated. Here, we are not interested as much in an inherent analysis of the errors with the aim of creating an accurate model, but rather in designing, to a first approximation, a sort of classification in order to help in the selection of the most suitable cases for validation purposes. Furthermore, we assume that the mathematical model of the antennas and, in case, of the structure on which those are installed, is an accurate representation of the real-world configuration, except for details small enough so that they affect only the reactive field, and have no effects on the radiated field pattern. The numerical error is independent from the point location (θ, ϕ) of the considered field and can be assumed to be constant all over the radiation pattern. Even in the spatial regions where the field becomes null, the error does not, since it remains as the statistic vectorial sum of the single error contributions, and is characterized by its mean and variance.

3.1.1 Physical Optics

Consider the PO approach, the field in every point results as the integration over the same N contributes on the considered surface. If we consider each of these contributes as affected by a local error, this leads to a global error that is the same for the field computed in every point in space and we can refer to it as a constant absolute error.

3.1.2 Geometrical/Uniform Theory of Diffraction

Generally, in the GTD/UTD approach only a limited number of rays contributes to field evaluation in the far field region. Besides, the nature of the problem itself (antennas are required to be as less obstructed as possible) imposes only one or few main contributes to exist, and consequently is reasonable to assume, to a first approximation, that the error is directly linked to the amplitude of this contributes. Hence, we may assume the relative error to be constant over the pattern. This approximation is not valid anymore, when we are in the presence of destructive interference between contributions of different rays, but generally this situation corresponds to isolated points (zeros of the radiation pattern) that will be of little significance on the overall quality of a method accuracy test.

3.1.3 Method of Moments

The MoM technique computes a coefficient matrix. Since each coefficient is obtained from integration of the field radiated by currents (of known amplitude, except for a scale factor to determine) that are distributed on a small portion of the structure,we can assume that, individually, the terms are

affected by a constant relative error, but variate singnificantly in amplitude according to the relative positioning of currents and point of observation. Thus, the solution of the linear system generates an error that is linked to the amplitude level of the currents that are determined by system itself but has intermediate characteristics with respect to the previous cases. Currents are, in turn, integrated to generate field values; therefore, associated errors add up in a statistical sense, while currents add up or subtract depending on the observation direction, resulting in an overall error that is, even if smaller in an absolute sense, more sensitive in lowly lit areas with respect to highly lit ones.
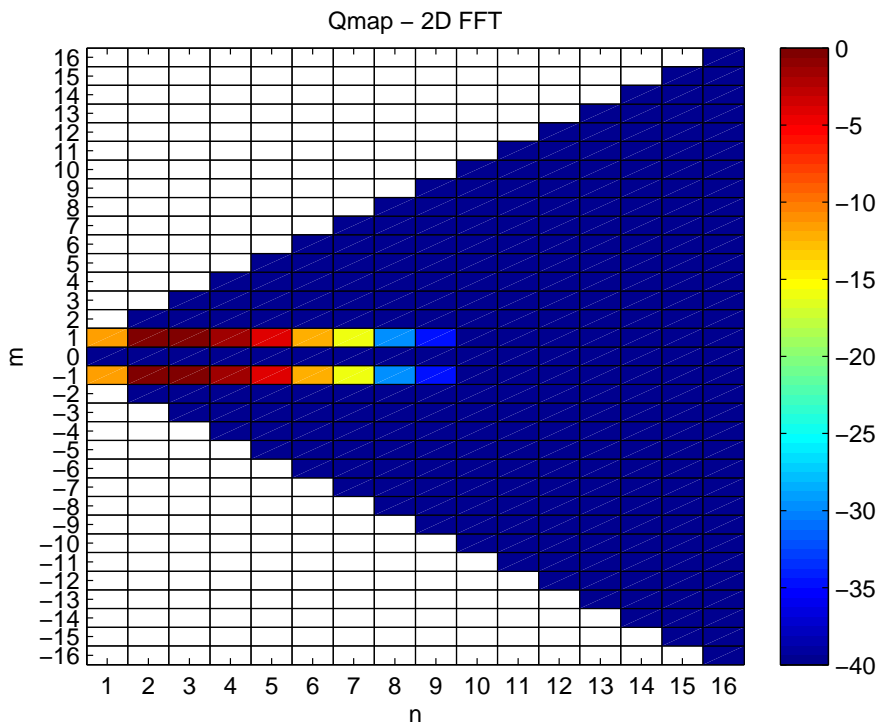
Figure 3.1: Qmap of a circular antenna pattern

3.2 Spherical wave expansion

In order to simulate numerical errors as decribed before, we introduce the methodology of spherical wave expansion as a medium to replicate and display radiation pattern of simple antennas. For an extensive discussion of the matter, we refer to [9]. This methodology allows us to describe the electromagnetic field as a superposition of spherical waves:

$$\mathbf{E}(r,\theta,\phi) = k\sqrt{Z} \sum_{s=1}^{2} \sum_{n=1}^{N} \sum_{m=-n}^{n} Q_{smn}^{c} \mathbf{F}_{smn}^{c}(r,\theta,\phi) \tag{3.1}$$

where $Z = \sqrt{\mu/\varepsilon}$ is the characteristic impedance of the medium, N is the truncation number for the n index and $\mathbf{F}_{smn}$ are the spherical wave vector functions.

Our interest is focused on coefficients Q_{smn}, that could be represented in a Qmap as in Figure (3.1) for a circular antenna.
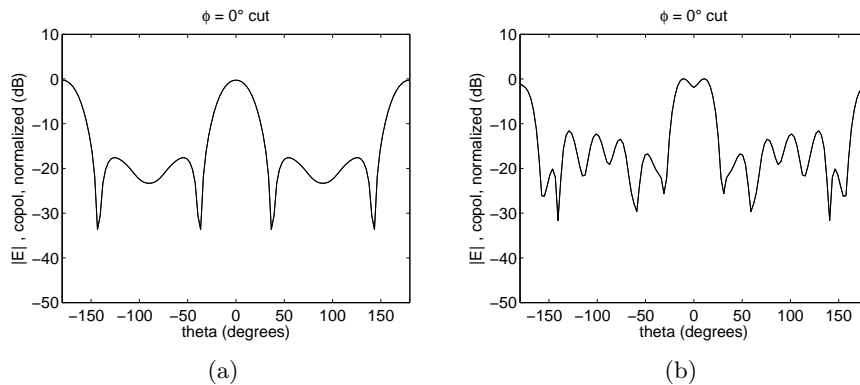
Figure 3.2: Antenna Pattern

3.3 Antenna Radiation Pattern

In order to achieve the wanted results, we simulate different antenna patterns and add to them numerical errors linked to different CEM techniques as supposed in Section (3.1). We are interested in working on different kinds of pattern to discover which one is more fitting for a particular validation procedure.

The antenna under analysis is a circular antenna whose pattern originates from Q coefficients of the spherical wave expansion.

Smooth pattern

The pattern obtained in this manner results to be particularly smooth and a ϕ-cut is represented in Figure (3.2 a). From now on, we will refer to it as Pattern 1.

Non-Smooth pattern

To obtain a pattern with different characteristics, we add noise to the latter; in this way we obtain a more indented shape and a ϕ-cut is shown in Figure(3.2 b). Similarly to the previous case, we will refer to it as Pattern 2.

34

3.4 Error modelling

Errors as described in Section (1.1), are applied on patterns under analysis, by operating on the coefficients Q_{mn} of the spherical wave expansion.

3.4.1 Absolute error

To introduce a constant absolute error on the radiation pattern, we are interested in modifying low frequency components, as they are responsible for the trend of the slowly varying features of the field.

Therefore, we operate on the coefficients as follows:

$$\boxed{Q_{A_{mn}} = Q_{mn} + \varepsilon} \tag{3.2}$$

where

$$\varepsilon = C_A \cdot f_g(n) \cdot u \tag{3.3}$$

results from a uniform complex stocastic process weighted by a gaussian distribution that is function of n index, and C_A is a multiplicative constant in the order of magnitude of 10^{-4}.

$$f_g(n) = \frac{1}{\sigma \sqrt{2\pi}} \exp \left\{ -\frac{(n - \mu)^2}{2\sigma^2} \right\} \tag{3.4}$$

This is done to achieve a distribution of the error that better represents its physical behaviour. As sigma increases, the gaussian enlarges and more coefficients are involved as depicted in Figure (3.4) and (3.5).

3.4.2 Relative error

To introduce a constant relative error on the radiation pattern we operate on the coefficients as follows:

$$\boxed{Q_{R_{mn}} = Q_{mn}(1 + \varepsilon)} \tag{3.5}$$

where $\varepsilon = C_R \cdot u$ result from a uniform complex stocastic process multiplied by a constant C_R. In this way, each coefficient is affected by an error that is proportional to its value, and the Qmap modifies as in Figure (3.6).
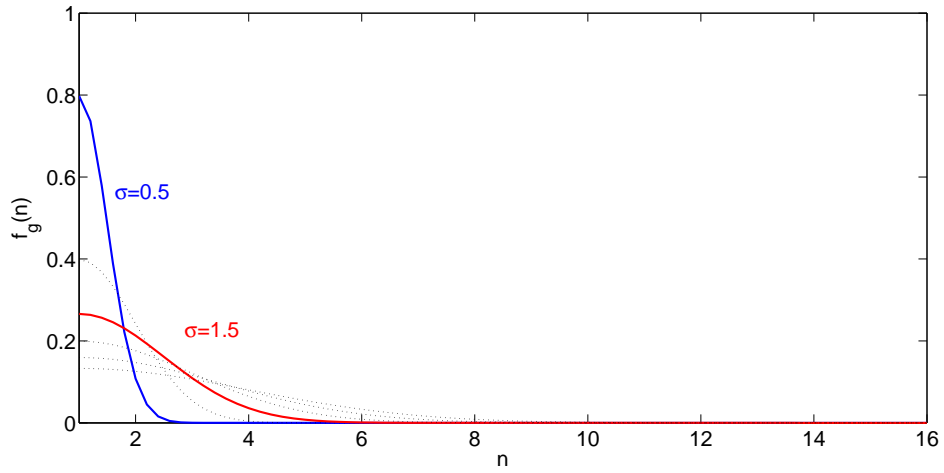
Figure 3.3: Weight function for different values of σ.
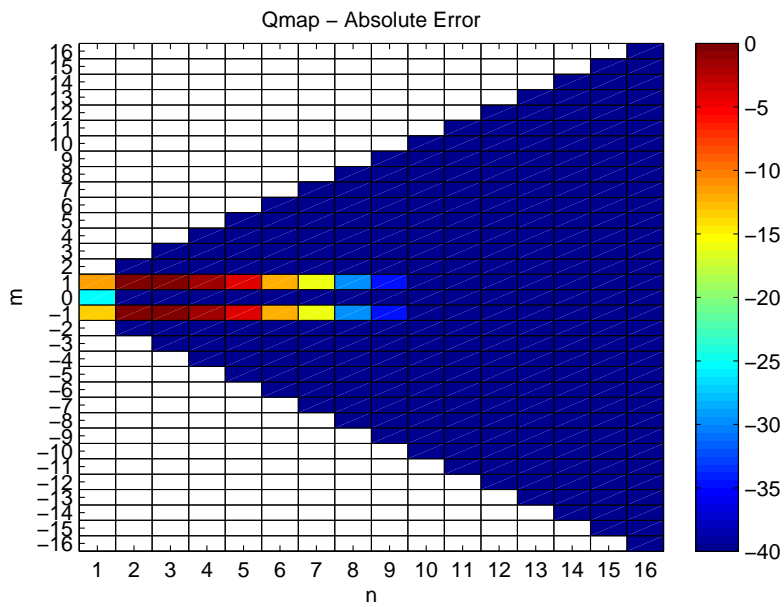
Figure 3.4: Modified Qmap for $\sigma = 0.5$
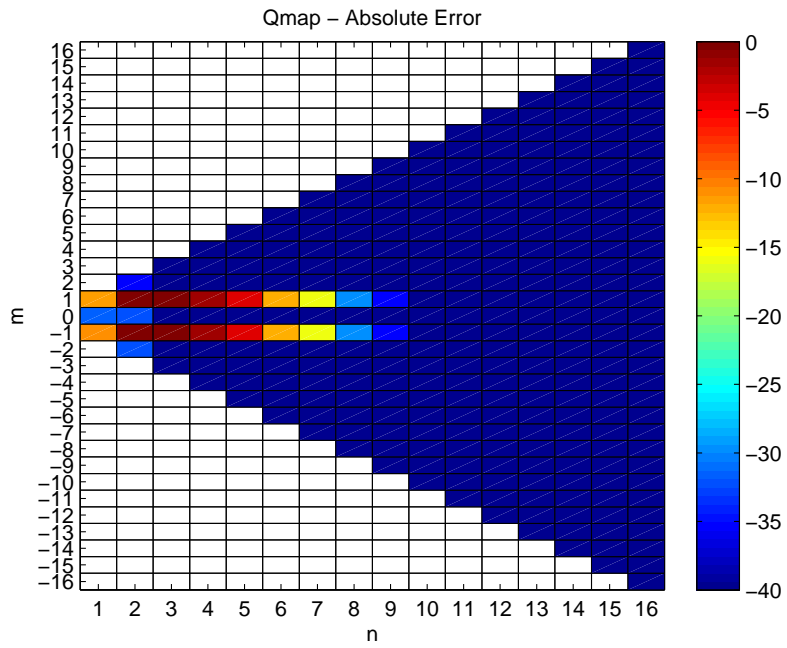
Figure 3.5: Modified Qmap for $\sigma = 1.5$
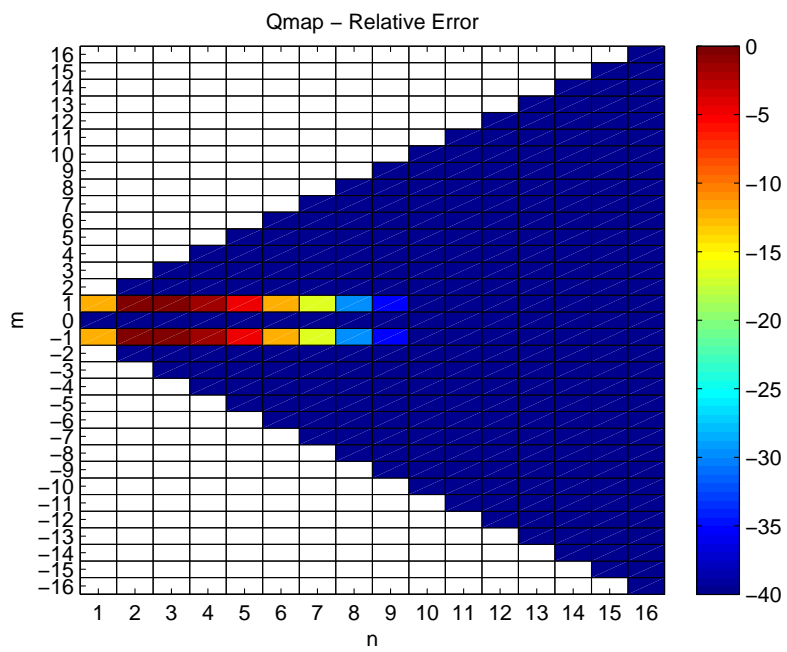
Figure 3.6: Modified Qmap

3.5 Configuration setup

We recall metrics of interest introduced in Chapter (2): Amplitude Difference Measure (ADM), Feature Difference Measure (FDM), Global Difference Measure (GDM), Normalized Relative Deviation for Low Frequencies ($RRLF$), for High Frequencies ($RRHF$) and Global Normalized Relative Deviation (RR). Metrics are gathered in two sets labeled Metric Set 1 and Metric Set 2 (see Table (3.1) and (3.2)), and for their computation we will refer to the simulated field, smooth or not, as the reference one, while the field reconstructed with added errors will be considered as the perturbed one.

Metric Set 1		
ADM	FDM	GDM

Table 3.1: Metric Set 1

Metric Set 2		
RRLF	RRHF	RR

Table 3.2: Metric Set 2

Furthermore, for reasons of clarity, we classify all cases under test and will refer to them according to Table (3.3); (e.g. a smooth pattern affected by absolute error will be referred to as Config 1).

	Pattern 1	Pattern 2
Absolute error	Config 1	Config 2
Relative error	Config 3	Config 4

Table 3.3: Reference Table
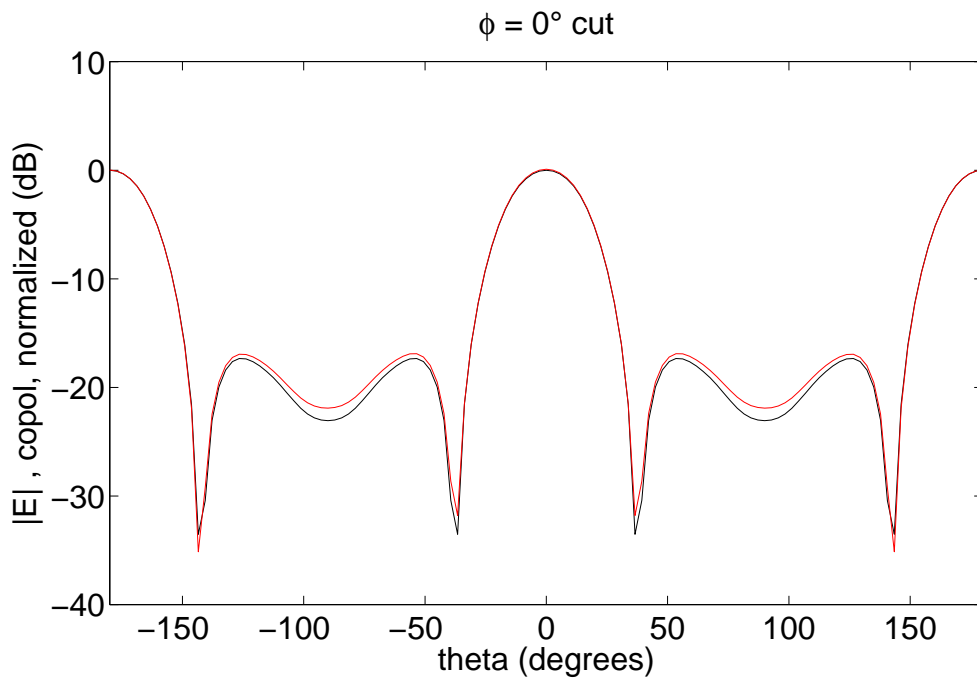
Figure 3.7: Config 1

Figure 3.8: Config 1

39

$\phi = 0°$ cut

Figure 3.9: Config 3

$\phi = 90°$ cut
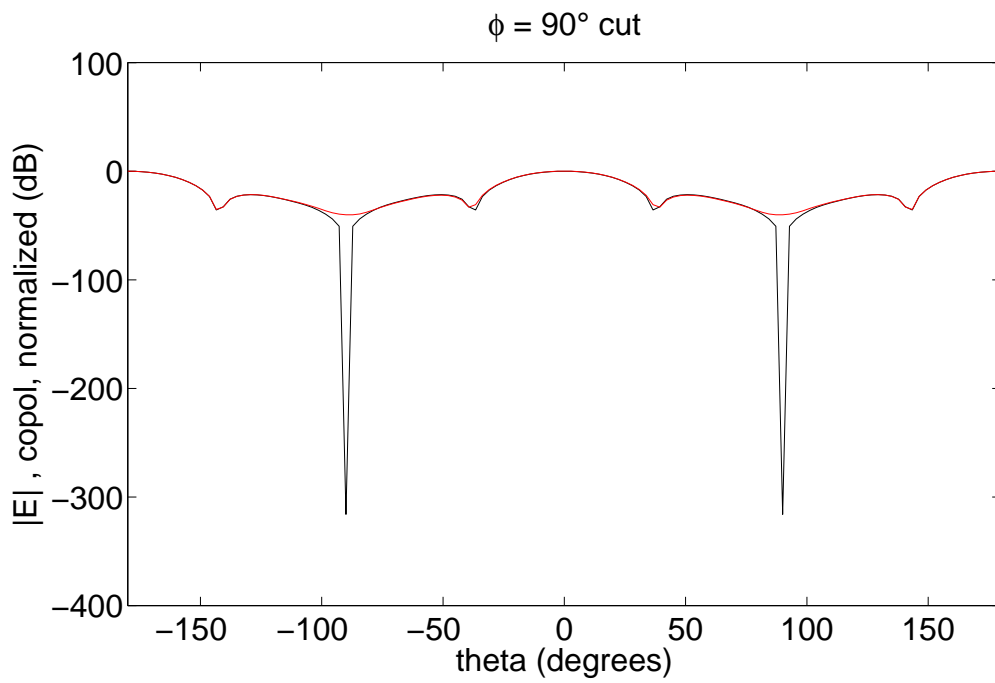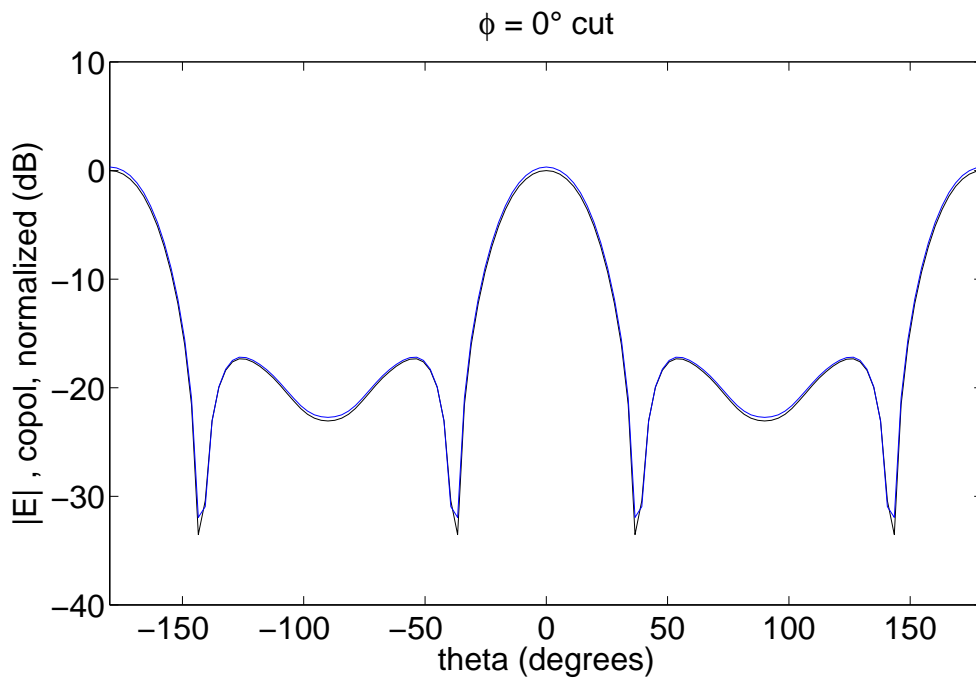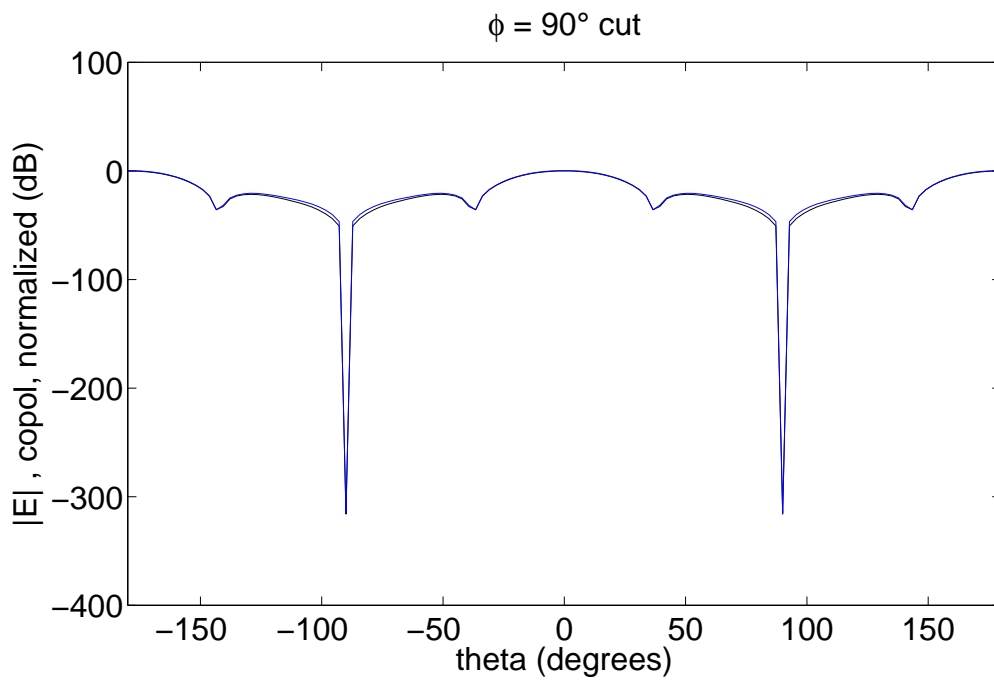
Figure 3.10: Config 3

40
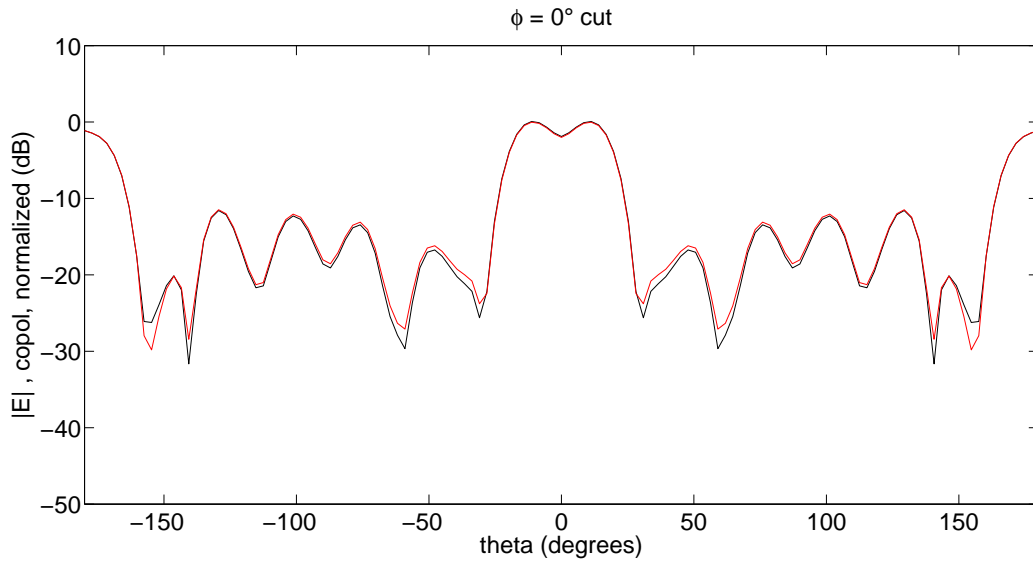
Figure 3.11: Config 2
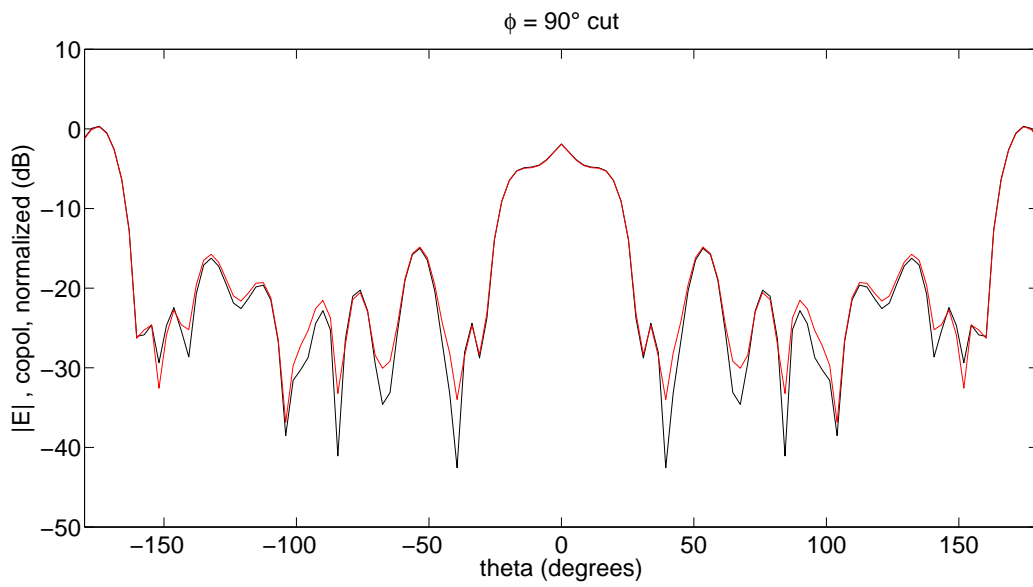
Figure 3.12: Config 2

41
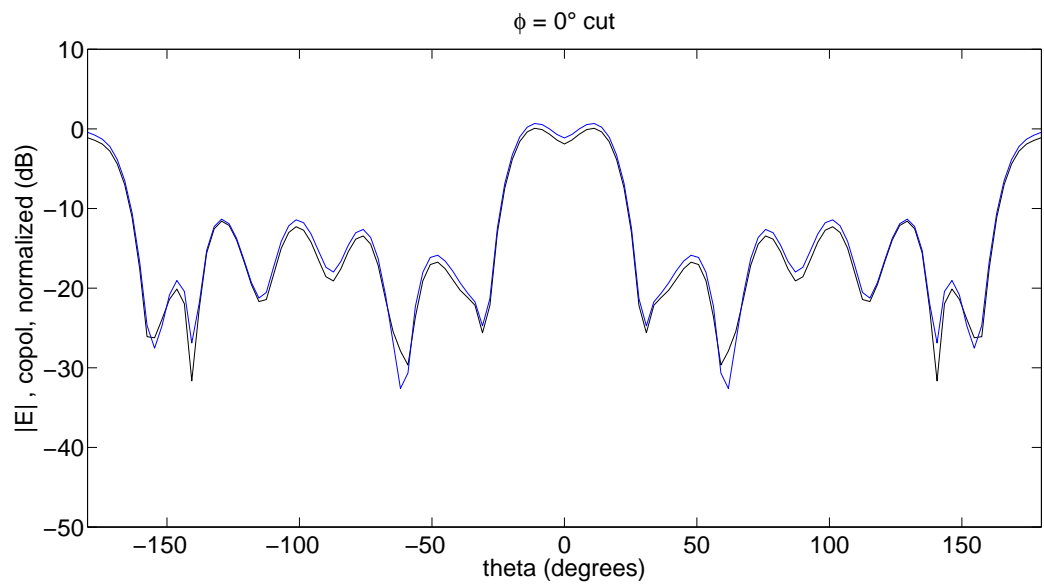
Figure 3.13: Config 4
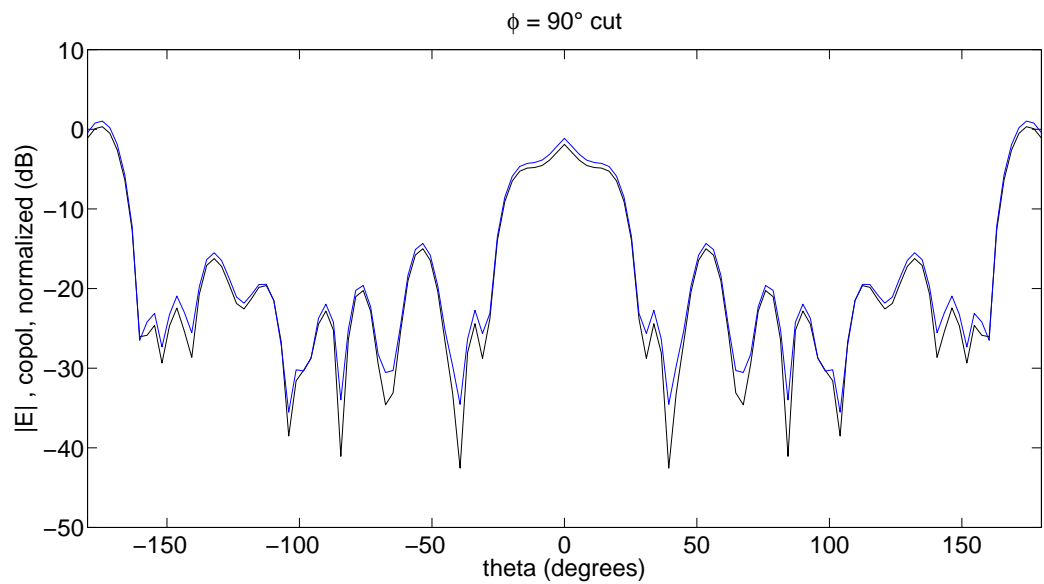
Figure 3.14: Config 4

42
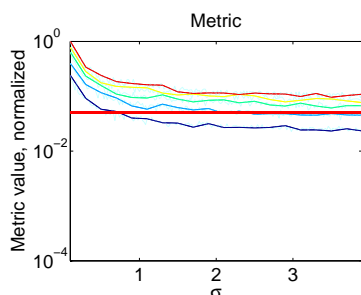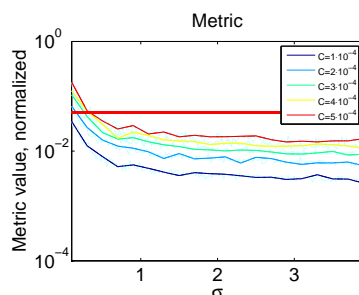
Figure 3.15: Config 1   Figure 3.16: Config 2

Figure 3.17: Intra-Metric Comparison

3.6   Intra-Metric Comparison

The purpose of the following section is to work simultaneously on both Pattern 1 and Pattern 2, by adding either an absolute or a relative error on the pattern, and comparing the values of the same metrics in the two cases, in order to discover which configuration has a stronger response to the induced perturbation.

3.6.1   Decisional Procedure

We are interested in introducing a procedure to be followed with the aim to discern between patterns candidated as reference for the validation procedure of an electromagnetic model.

Method steps

- **Metric values computation**: we compute metric values on varying C_A or C_R for several ϕ-cuts of both smooth and non-smooth patterns. In the case of absolute error with respect to relative error we have an additional degree of freedom that is σ.

- **Normalized plot**: in order to be able to compare the results, we plot, for each set of metrics, the normalized values of the metrics for different values of the multiplicative constant C_A or C_R. Plots related to Config 1 and Config 2 will be functions of σ.

- **Metric values spanning**: for each pattern and for each metric, we span the metric value domain, and for each ordinate value we compute the minimum C that allows the plot to reach that value (see Fig.(3.17) and (3.20)).

- **"Minimum C" comparison**: We compare, for each metric in a set, the minimum values of C, among Pattern 1 and Pattern 2, which
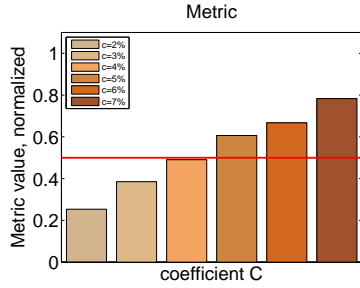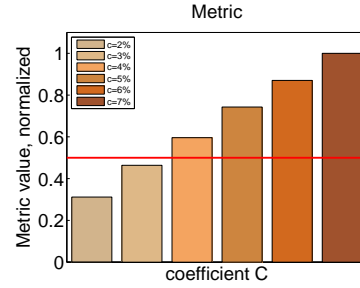
43

Figure 3.18: Config 3

Figure 3.19: Config 4

Figure 3.20: Intra-Metric Comparison

allow to reach a determined metric value and note which pattern is responsible for it. We report the results in a table, where the entries are the frequencies of the cases for which a "minimum C" belongs to a pattern or to both of them.

- **Table filling**:

| Pattern | Metric | | | | | |
| | Set 1 | | | Set 2 | | |
	ADM	FDM	GDM	RRLF	RRHF	RR
Pattern 1	●	●	●	●	●	●
Pattern 1 & 2	●	●	●	●	●	●
Pattern 2	●	●	●	●	●	●

Table 3.4: ϕ cut

- **Results drawing**: we refer to values in the table to establish which correlation can be observed between a pattern and a specific type of error. In other words, we count how many times a configuration is responsible of a "minimum C" with respect to the other in order to discuss the sensitivity of a pattern to an error. Finally, relying on these results, we will be able to conclude about the suitability of a specific configuration for validation purposes.

3.6.2 Analysis

We show side by side plots relative to the the same metric value for different configurations, for a first visual comparison in Figure (3.21), (3.22), (3.23), (3.24), (3.25) and (3.26).

Absolute error
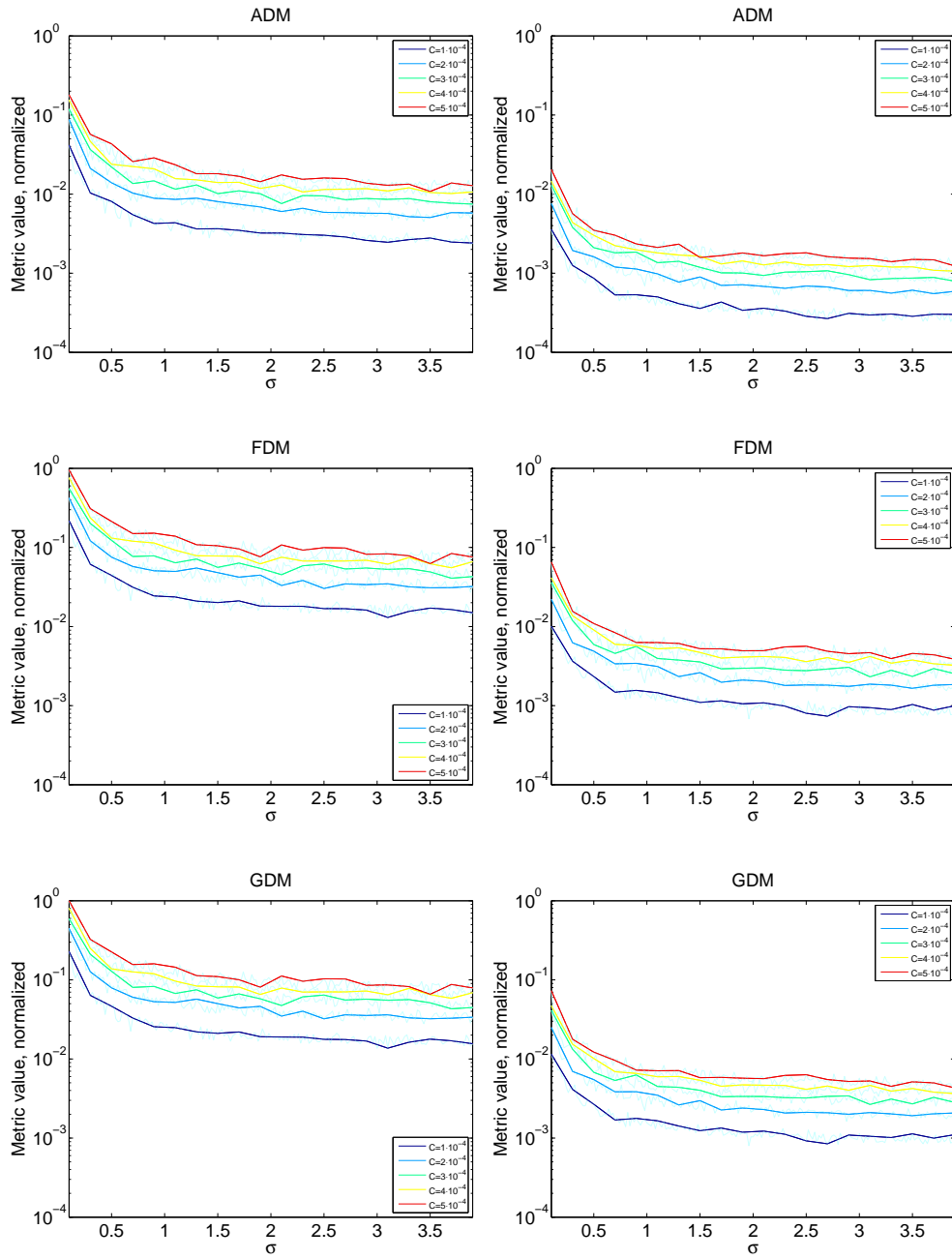
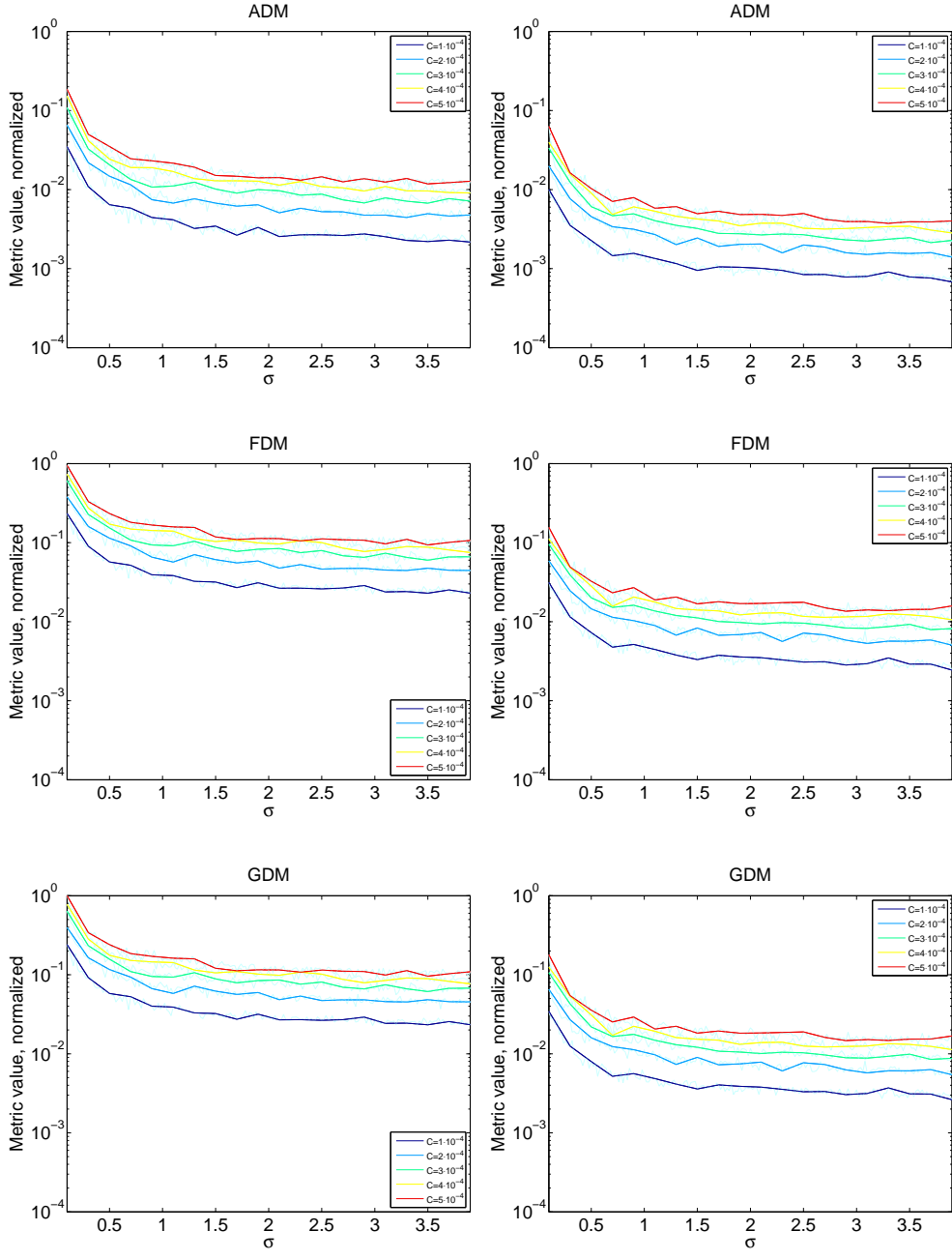Figure 3.21: Cut $\phi = 0°$: Pattern 1 vs. Pattern 2 Absolute error response for Metric Set 1.

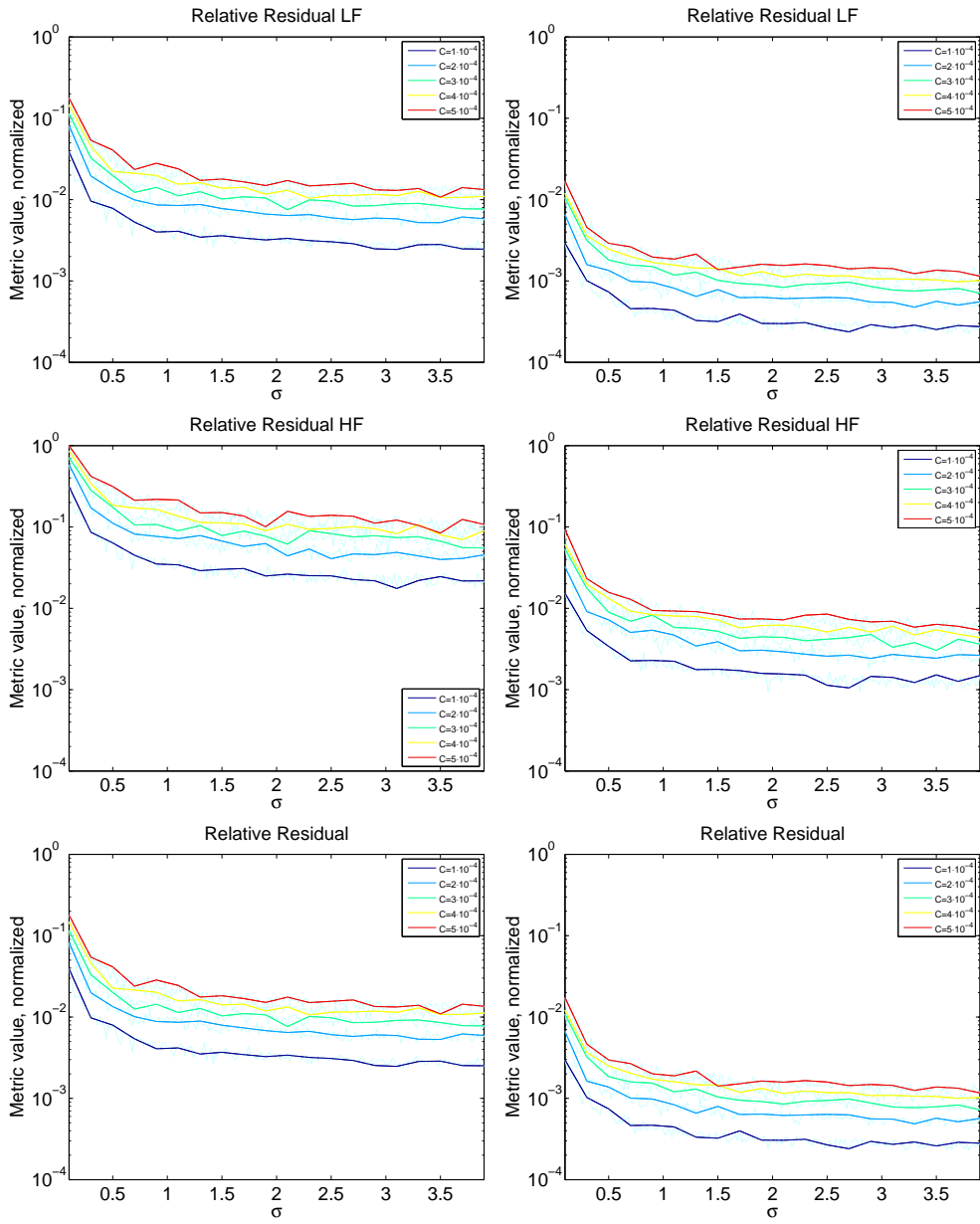Figure 3.22: Cut $\phi = 90°$: Pattern 1 vs. Pattern 2 Absolute error response for Metric Set 1.

Figure 3.23: Cut $\phi = 0°$: Pattern 1 vs. Pattern 2 Absolute error response for Metric Set 2.

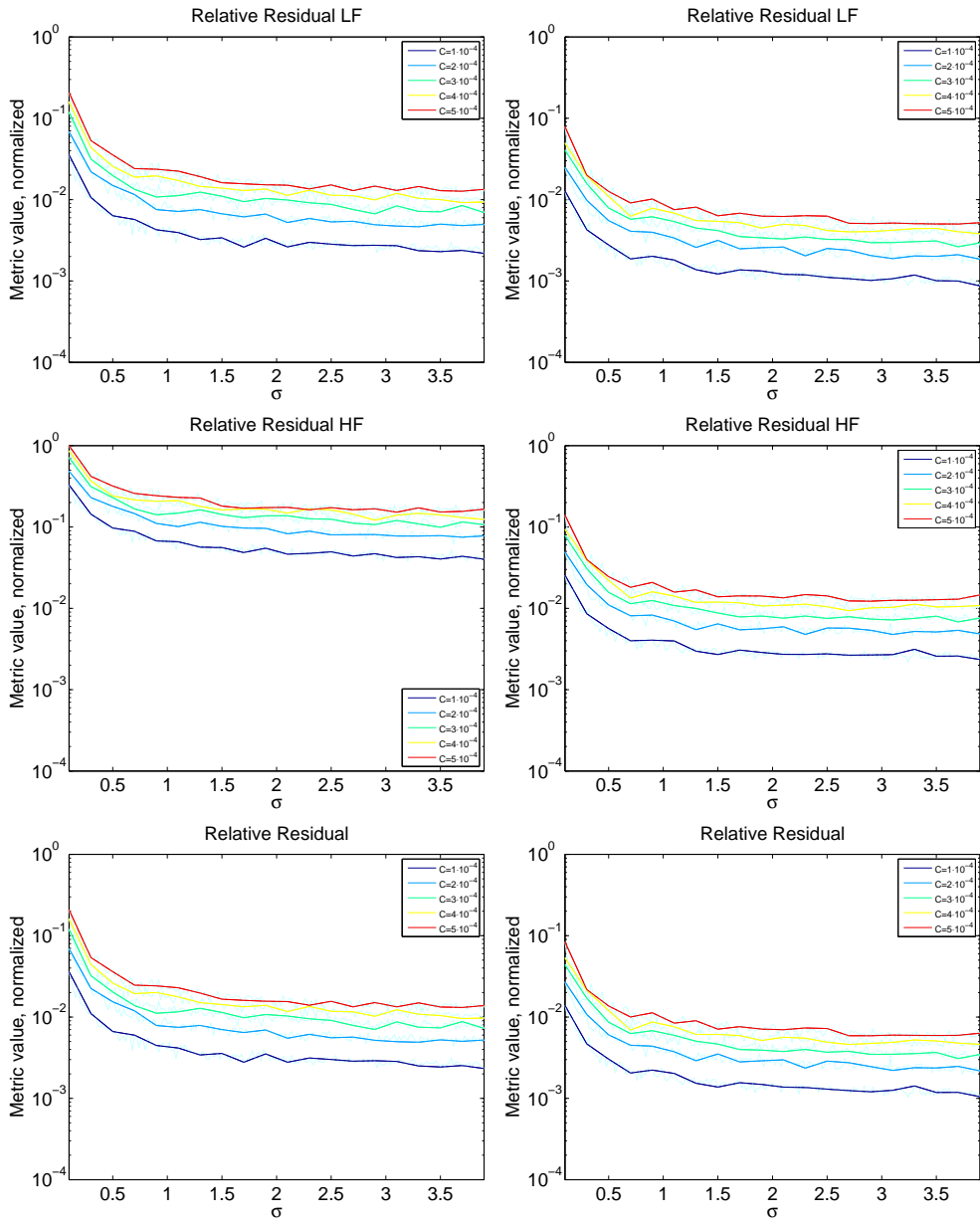Figure 3.24: Cut $\phi = 90°$: Pattern 1 vs. Pattern 2 Absolute error response for Metric Set 2.
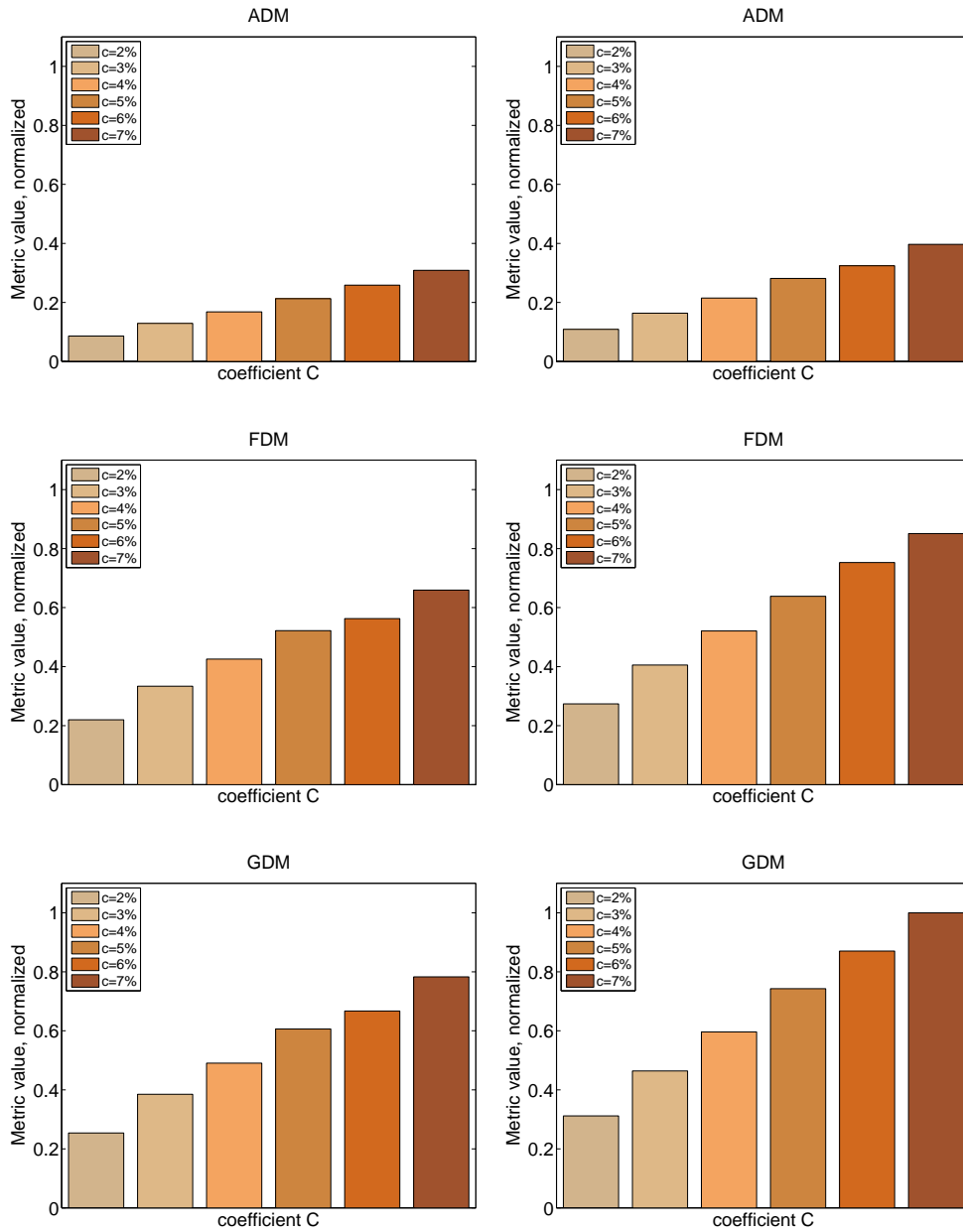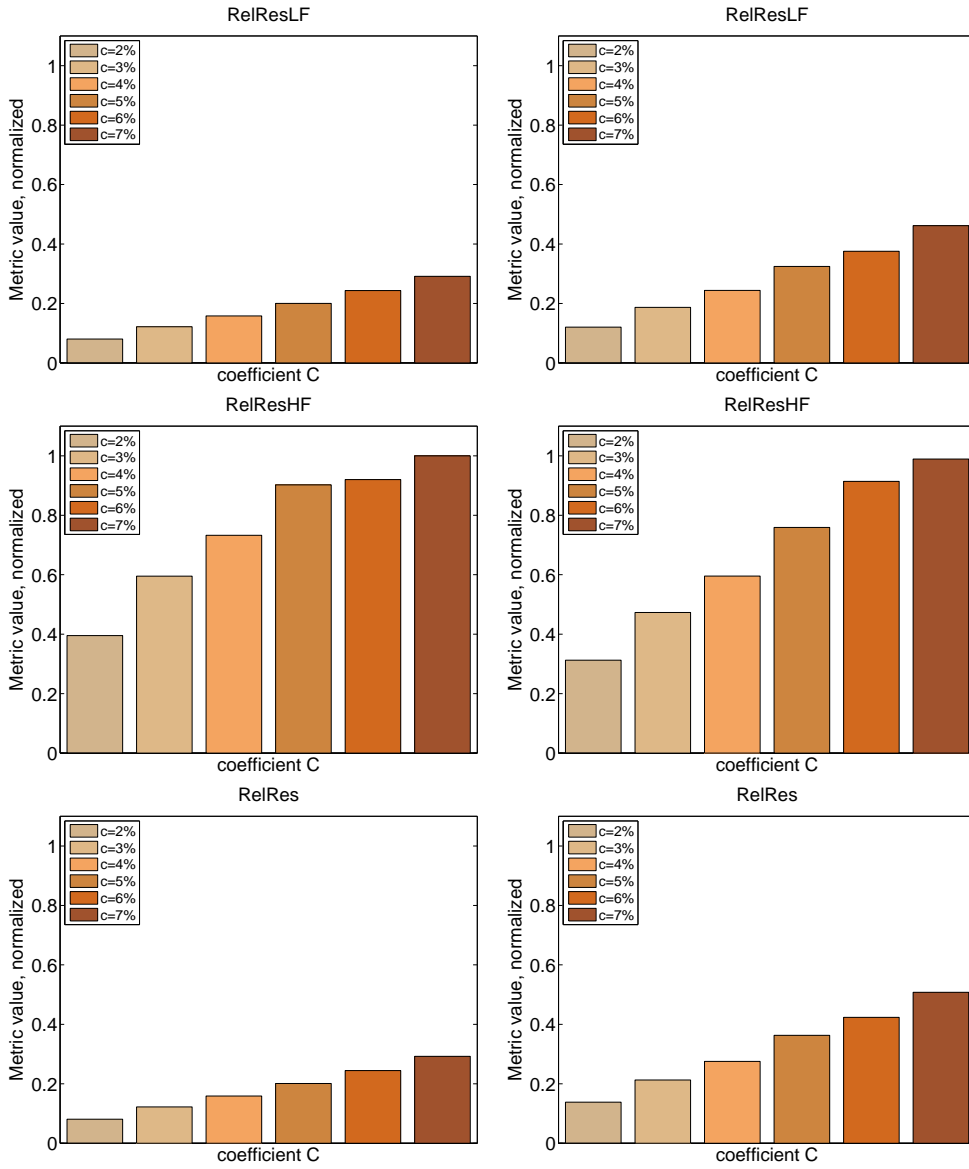
Relative error

Figure 3.25: Cut $\phi = 90°$: Pattern 1 vs. Pattern 2 Relative error response for Metric set 1.

Figure 3.26: Cut $\phi = 90°$: Pattern 1 vs. Pattern 2 Relative error response for Metric Set 2.

3.6.3 Results

Absolute error

Results of the analysis for Config 1 vs. Config 2 are reported in Table(3.5) and (3.6):

Pattern	Metric					
	Set 1			Set 2		
Pattern	ADM	FDM	GDM	RRLF	RRHF	RR
Pattern 1	23%	12%	13%	15%	9%	15%
Pattern 1 & 2	77%	88%	87%	85%	91%	85%
Pattern 2	0%	0%	0%	0%	0%	0%

Table 3.5: Cut $\phi = 0$

Pattern	Metric					
	Set 1			Set 2		
Pattern	ADM	FDM	GDM	RRLF	RRHF	RR
Pattern 1	41%	17%	17%	31%	12%	32%
Pattern 1 & 2	59%	83%	83%	69%	88%	68%
Pattern 2	0%	0%	0%	0%	0%	0%

Table 3.6: Cut $\phi = 90$

Referring to tables, we can conclude that both set of metrics report an higher sensitivity to absolute error in the case of Pattern 1 with respect to Pattern 2. According to these results, in order to validate a simulation based on a CEM technique that introduces this kind of numerical error (PO in our hypothesis), a smooth radiation pattern would be required.

To obtain such a radiation pattern, the measurement setup has to involve an antenna which is not affected by the surrounding structures and scattering effects should be avoided.

Relative error

Results of the analysis for Config 3 vs. Config 4 are reported in Table(3.7) for cut $\phi = 90$ of interest.

Referring to table, we can conclude that metrics report with a clear evidence an higher sensitivity to relative error in the case of Pattern 2 with respect to Pattern 1. According to these results, in order to validate a simulation based on a CEM technique that introduces this kind of numerical

	Metric					
	Set 1			Set 2		
Pattern	ADM	FDM	GDM	RRLF	RRHF	RR
Pattern 1	0%	0%	0%	0%	16%	0%
Pattern 1 & 2	32%	68%	76%	68%	84%	73%
Pattern 2	68%	32%	24%	32%	0%	27%

Table 3.7: Cut $\phi = 90$

error (GTD/UTD in our hypothesis), a non-smooth radiation pattern would be required.

In fact, considering the pointwise nature of the error that affects that technique, a more indented pattern is required and thus an antenna measurement configuration affected by the surrounding environment.

3.7 Inter-Metrics Comparison

Observing plots in Figure (3.21), (3.22), (3.23) and (3.24) it appears evident that, except for shifts in amplitude, the trends of chosen metrics result to be very similar on increasing σ for mostly all the cases under discussion. The goal of this section is to discover if a set of metrics, or a single metric belonging to a set, has a stronger response to a given type of error in relation to a selected pattern, with respect to the other metrics and can therefore be preferred to the latter for this kind of analysis.

3.7.1 Method

In order to do as stated, we operate as follows:

- **"C-selection"**: for each pattern and each metric we select the plot relative to the same fixed multiplicative coefficient C (e.g. $C = 5 \cdot 10^{-4}$).

- **Normalization**: we normalize for the maximum value among all the metric values, so that we obtain comparable amplitudes for all the metrics.

- **Plotting**: for each selected pattern and ϕ-cut we plot the metrics belonging to the two sets on the same graph.

3.7.2 Analysis

Refer to Figure (3.27) and (3.28), those are obtained following the methodology described in Section (3.6). As noticed before, the trend of the different metrics is very similar for the different cases, but by overlapping plots on the same graph, another important characteristic is drawn to attention. In fact, if we focus on FDM and GDM with respect to $RRLF$ and RR, we can notice that when referring to Pattern 1 there is an evident gap between them, whereas they were almost matching in the case of Pattern 2.
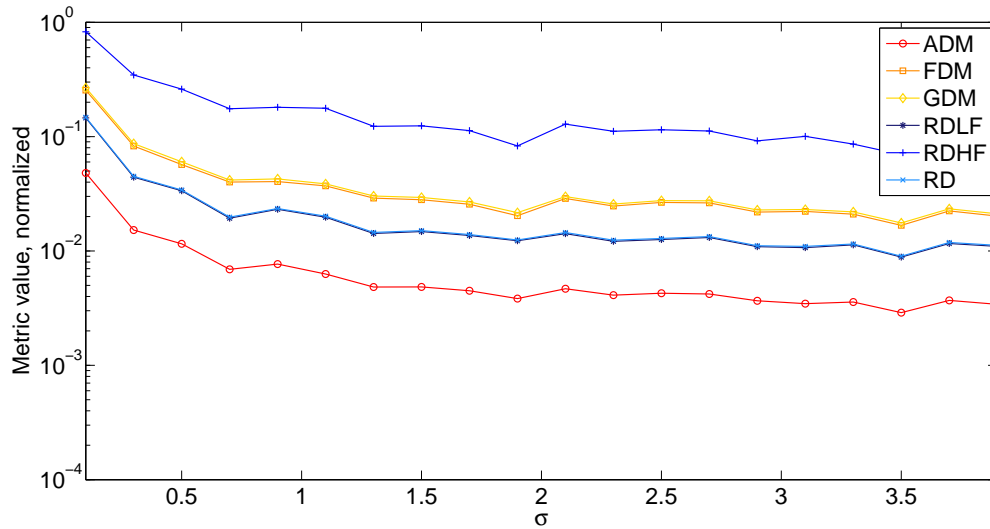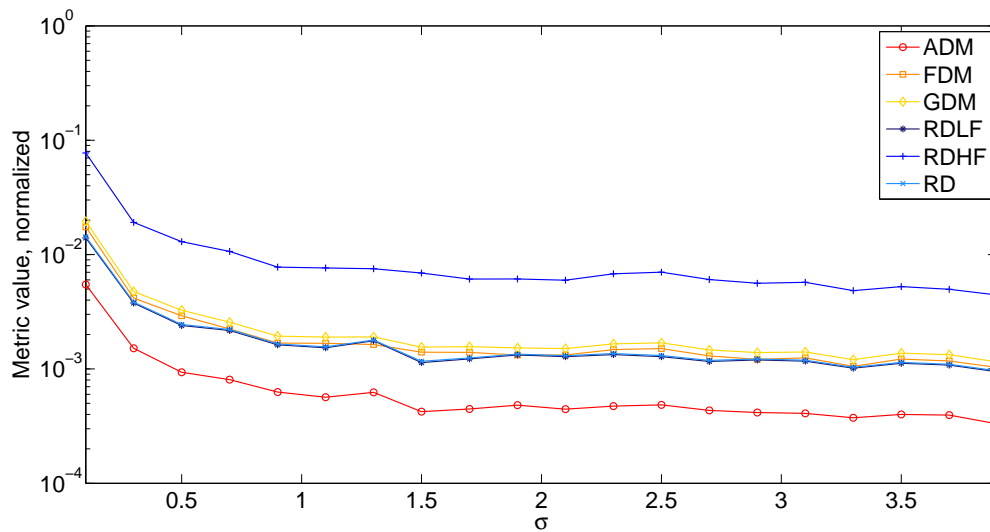
Figure 3.27: Config 1 - $\phi = 0$

Figure 3.28: Config 2 - $\phi = 0$

In order to quantify what graphycally observed, we measure the percent variation of FDM and GDM with respect to $RRLF$ and RR for both the patterns under test, and the results are shown in Table (3.10) and (3.11).

Pattern 1	ADM	FDM	GDM	RRLF	RRHF	RR
$\sigma = 0.3$	0.015	0.083	0.087	0.044	0.346	0.044
$\sigma = 0.5$	0.012	0.057	0.060	0.034	0.260	0.035
$\sigma = 0.9$	0.008	0.040	0.043	0.024	0.180	0.025

Table 3.8: Config 1 - $\phi = 0$, data for fixed σ

Pattern 2	ADM	FDM	GDM	RRLF	RRHF	RR
$\sigma = 0.3$	0.002	0.004	0.005	0.004	0.019	0.004
$\sigma = 0.5$	0.001	0.003	0.003	0.003	0.013	0.003
$\sigma = 0.9$	0.001	0.002	0.002	0.002	0.008	0.002

Table 3.9: Config 2 - $\phi = 0$, data for fixed σ

3.7.3 Results

The results of the analysis lead us to conclude that in the case of an absolute error introduced on the pattern, metrics related to the first set respond in a more effective way if compared to those belonging to the second one. In fact, if we observe the percentage gain of FDM and GDM with respect to $RRLF$ and RR, we can notice a strong variation while moving from $Pattern 2$ to $Pattern 1$, which was selected as best fitting the validation needs in case of absolute error. Thus, we can conclude that for a smooth pattern affected with an absolute error, the first set of metrics can be preferred to the second one as a mean for validation purposes.

Pattern 1	FDM vs. RRLF	FDM vs. RR	GDM vs. RRLF	GDM vs. RR
$\sigma = 0.3$	0.89%	0.89%	0.98%	0.98%
$\sigma = 0.5$	0.68%	0.63%	0.76%	0.71%
$\sigma = 0.9$	0.67%	0.60%	0.79%	0.72%

Table 3.10: Config 1 - $\phi = 0$, inter-metric comparison

Pattern 2	FDM vs. RRLF	FDM vs. RR	GDM vs. RRLF	GDM vs. RR
$\sigma = 0.3$	0.07%	0.07%	0.22%	0.22%
$\sigma = 0.5$	0.21%	0.21%	0.36%	0.36%
$\sigma = 0.9$	0.02%	0.02%	0.17%	0.17%

Table 3.11: Config 2 - $\phi = 0$, inter-metric comparison

Chapter 4

Tool simulated patterns - Analysis and Comparison

4.1 Introduction

The final purpose of this work is to study errors linked to CEM techniques, in order to be able to create measurement setups, that can provide critical configurations for the validation of electromagnetic modelling tools. The final measurement set-up we are interested in studying involves the mock-up of a satellite, with multiple antennas installed on it. To recreate this situation, a software modelling tool will simulate pattern of antennas installed on a cubical structure ($2m \times 2m \times 2m$), with the aim of reproducing and working on patterns that would be similar to the real-world ones. Simulation setup is reported in Figure (4.1). Two cube-antennas interfacing will be considered in this work. The first one, an helix antenna installed on a vertex of the cube, and the second one, two helix antennas installed on opposite vertices of the cubical structure. We will refer to the first set-up as SingleAntennaPattern and to the second as CombinedAntennaPattern. A software tool will provide MOM, PO and GTD simulations of both configurations. We will consider MOM model as the reference pattern, and PO-GTD models as perturbed fields to be validated in an hypothetical validation procedure.

First, we will conduct a further analysis on numerical errors, working on a reference radiation pattern that could be more similar to the real-world case. Second, we will study and compare PO and GTD modelling of both Single and Combined AntennaPattern, with the aim of understanding if the measurement configuration could result in a critical case for the model validation. Finally, we will realize an exemplifying application of a validation procedure, assuming the MOM model as reference pattern.
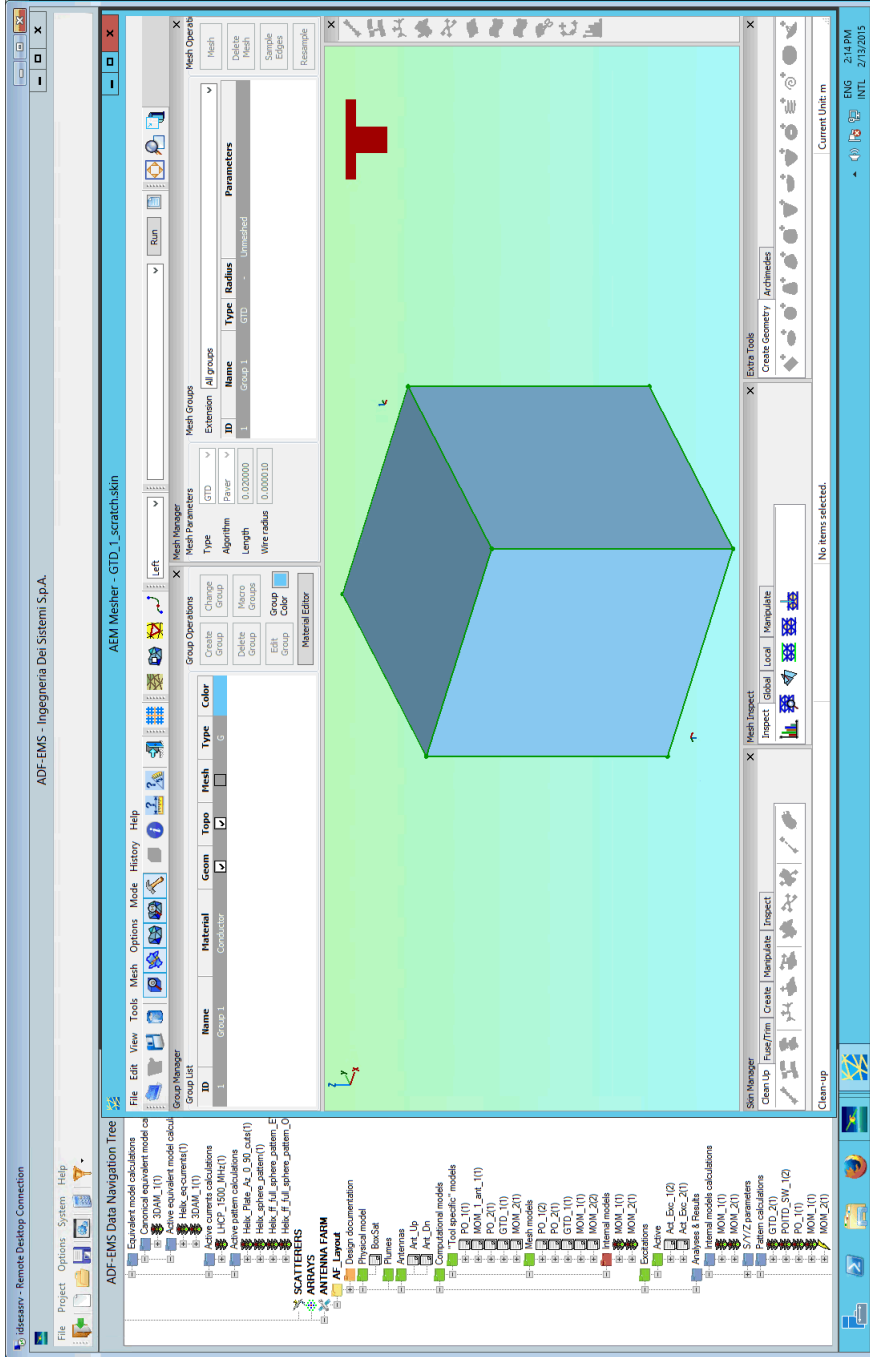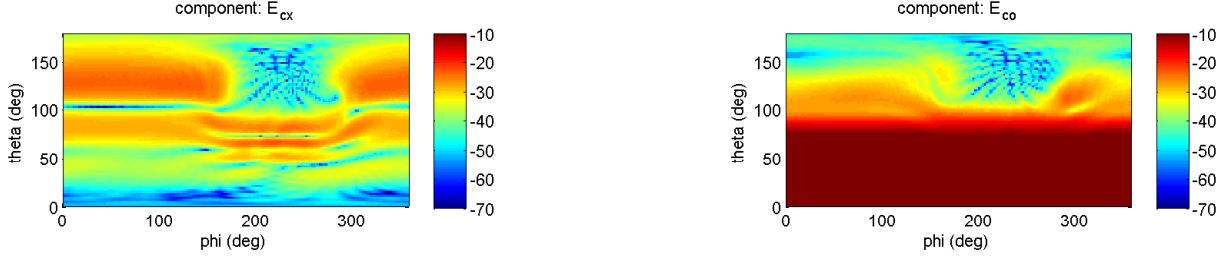
Figure 4.1: Simulation environment

Figure 4.2: Reference field components - (MOM)

	Absolute error	Relative error
SingleAntennaPattern	Config. 5	Config. 6

Table 4.1: Error modelling set-up

4.2 Intra-pattern Analysis

The first pattern under analysis is generated by an helix antenna installed on a vertex of a cubical structure. Here, we assume as reference pattern the one simulated via MOM modelling. It is interesting to observe how the cube creates a sort of shaded region, in which the electric field is very low in amplitude and its shape is influenced by some ripple effects. Field co-polar and cross-polar components are shown in Figure (4.2)

In Chapter (3), our interest was in discussing and comparing configurations related to two different patterns. Now, we focus on a set-up in which we work on the same pattern, by simulating different types of numerical error on it. We can refer to this study as intra-pattern analysis. Errors considered in this analysis are again an absolute and a relative error, that are now applied directly on the electric field values.

We will refer to configurations studied in this section according to Tab.(4.1).

4.2.1 Absolute error

We can model the absolute error on the radiation pattern as:

$$E_{abs} = E_0 + \varepsilon = E_0 + C_A \cdot u \qquad (4.1)$$

where C_A is a multiplicative coefficient and u results from a uniform complex stochastic process. An example of absolute error on a ϕ-cut of particular interest, since it falls in the spatial region shaded by the cube, is shown in Figure (4.3).
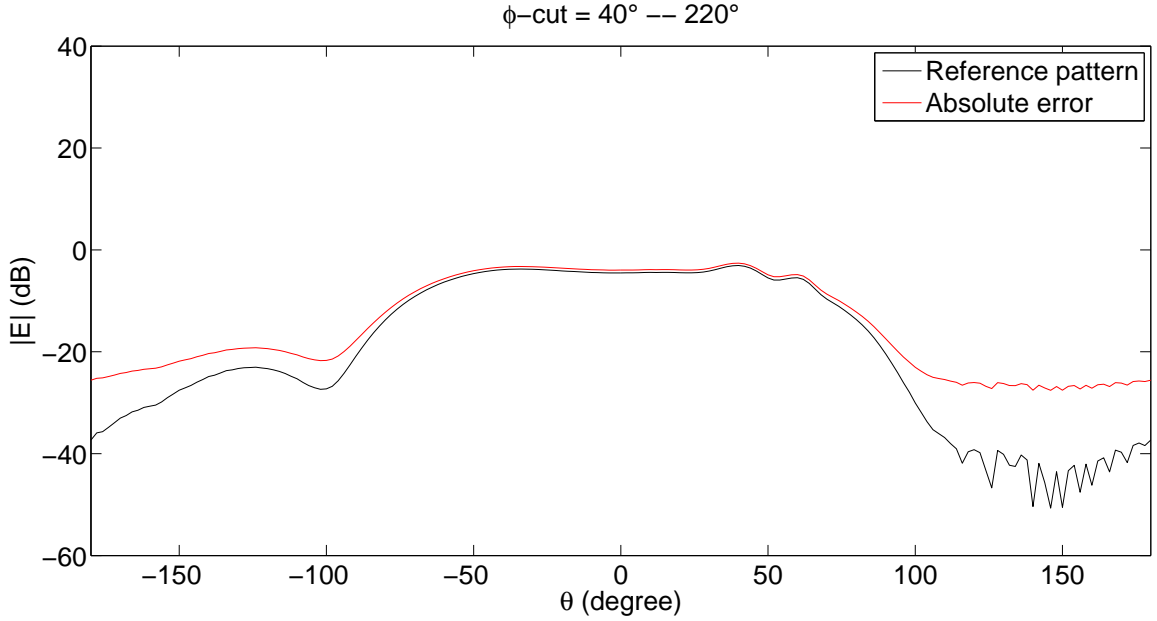
Figure 4.3: Absolute error on MOM Pattern

4.2.2 Relative error

We can model the relative error on the radiation pattern as:

$$E_{rel} = E_0(1 + \varepsilon) = E_0(1 + C_R \cdot u) \tag{4.2}$$

where C_R is a multiplicative coefficient and u results from a uniform complex stochastic process. An example of relative error on a ϕ-cut of particular interest, since it falls in the spatial region shaded by the cube, is shown in Figure(4.4).

4.2.3 Procedure

The following steps have to be followed in order to understand which kind of error causes the pattern to have a stronger response. The procedure is presented below.

- Metric selection: we select as metric for quantitative comparison of reference and modified field the Field Relative Residual:

$$\varepsilon_M = \sqrt{\frac{\iint_S |\tilde{E}(\theta, \phi) - E(\theta, \phi)|^2 dS}{\iint_S |E(\theta, \phi)|^2 dS}} \tag{4.3}$$

- Metric values computation: we compute metric values for both Config. 5 and Config. 6 on varying C_A and C_R respectively.

59
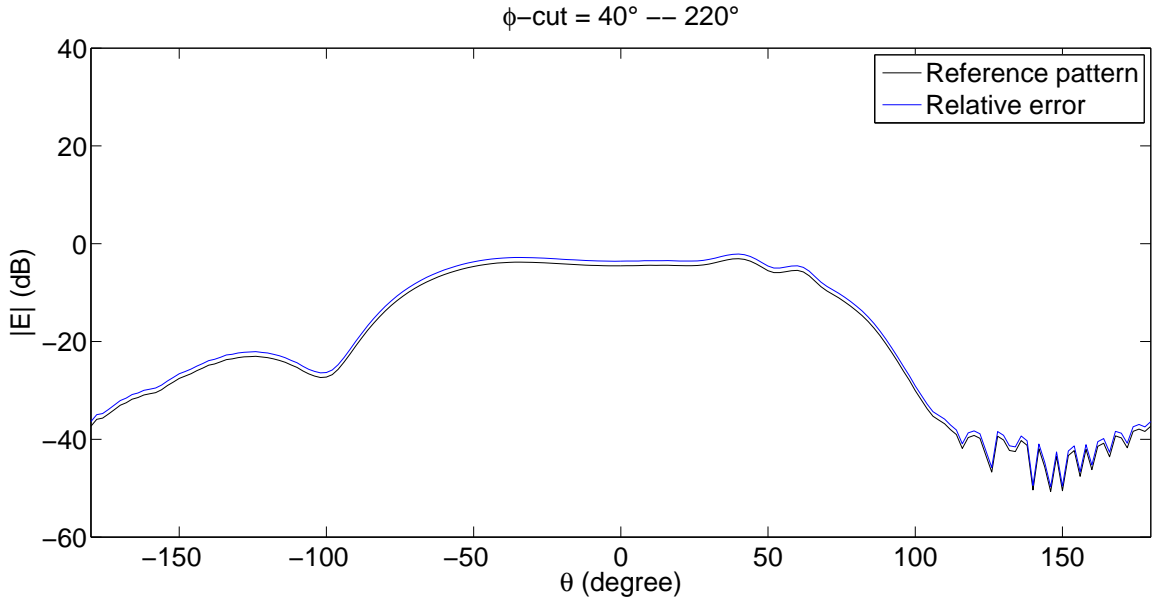
Figure 4.4: Relative error on MOM Pattern

- Coefficient evaluation: for a fixed computed metric value, we evaluate for which coefficient C_A and C_R this value is reached, respectively for Config. 5 and Config. 6. We repeat this step for several metric values to obtain a relation between the increase of coefficient values and the metric.

- Graphic representation: we plot the trend of the coeffcents on increasing metric values.

- Derivative analysis: we use derivative calculation as indicator of the variation of coeffcents C_A and C_R needed to provide the same metric increas.

4.2.4 Analysis

We proceed as indicated in Section(4.2.3), using as reference pattern InstalledPatternMOM. Absolute and relative errors are introduced on the same pattern on varying C_A and C_R, and the results are shown in Tab.(4.2) and in Figure (4.5).

Numerical error	Absolute error	Relative error
Derivative	6.01	17.80

Table 4.2: Derivative values

60
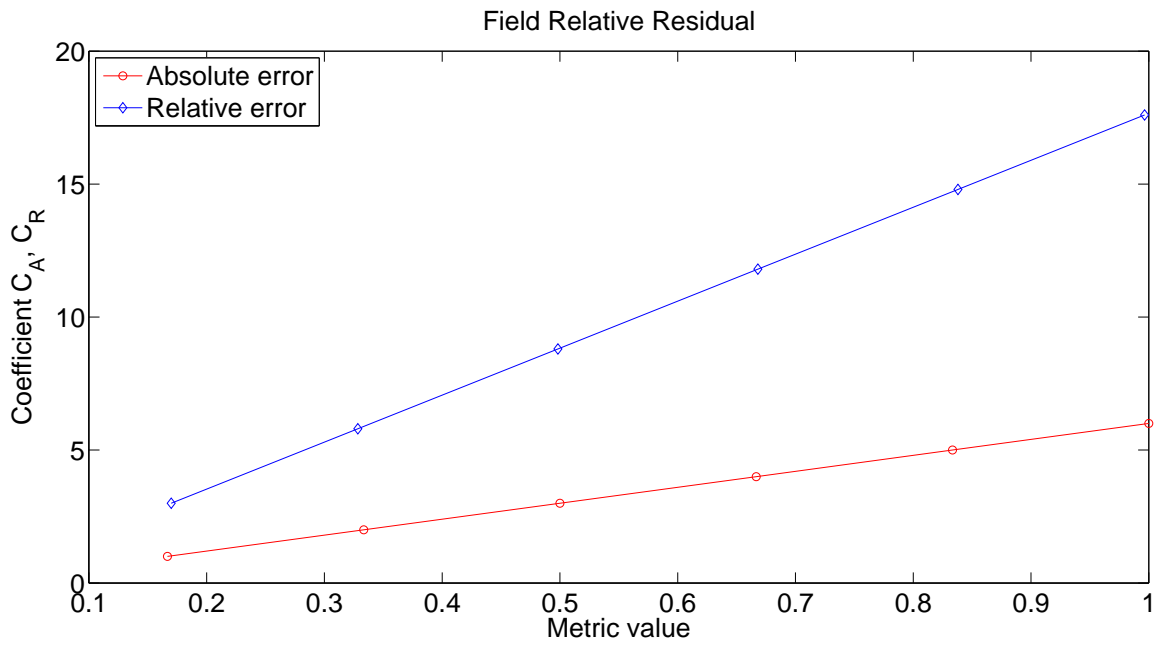
Figure 4.5: Coefficient trend

4.2.5 Conclusions

Referring to Tab.(4.2), we can notice that the derivative is greater in the case of a relative error introduced on the pattern with respect to the case of an absolute error. Thus, a minor increase in coefficient values is required to obtain the same variation in the metric value in the latter case, and we can conclude that this pattern is more sensitive to an absolute error with respect to a relative error. Hence, a pattern as this one, results to be a case of particular interest for the validation of a simulation based on a technique that introduces a numerical error, modeled as absolute, on the pattern.

4.3 Simulated patterns - Model sensitivity

Software tool used to generate the reference pattern, will provide us models, based on PO and GTD tecniques, of the same physical configuration. Radiation patterns obtained in this way are shown in Figure (4.2)-(4.6)-(4.7) for SingleAntennaPattern and in Figure (4.8)-(4.9)-(4.10) for CombinedAntennaPattern. We are interested in observing which mismatch is introduced by PO and GTD modelling with respect to the reference one, and which spatial region results particularly affected. As in the previous chapter, validation metrics will provide means to quantify and localize this disagreement.

4.3.1 Field simulation

SingleAntennaPattern

We can notice that the amplitude level of the electric field is very similar for these simulations, except for a region in which PO modelling introduces an evident ripple effect on the pattern.
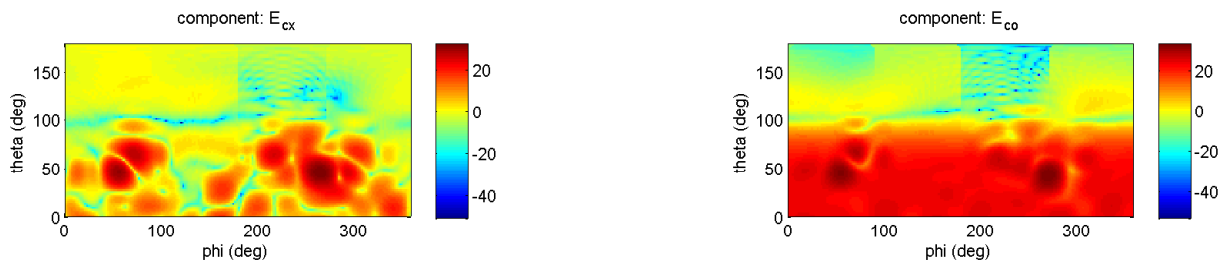
Figure 4.6: PO Components
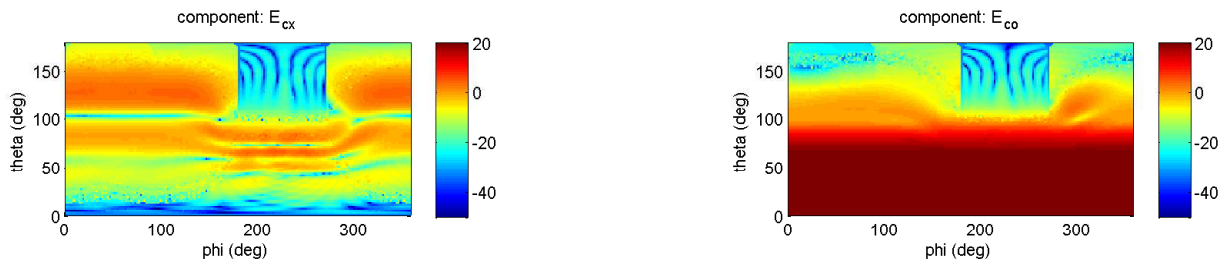
Figure 4.7: GTD Components

CombinedAntennaPattern
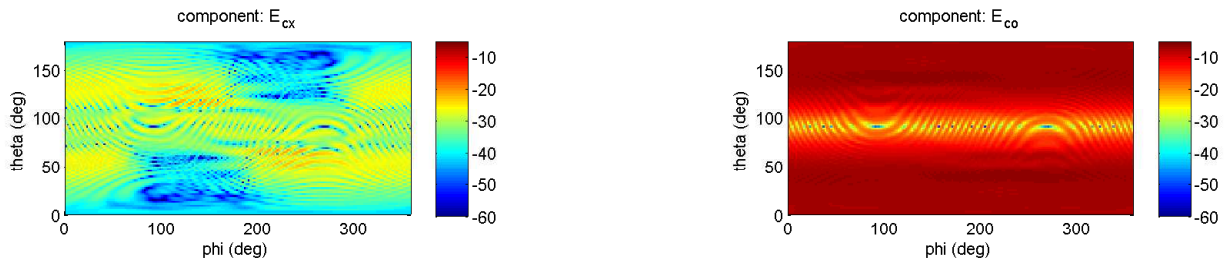
Figure 4.8: MOM components
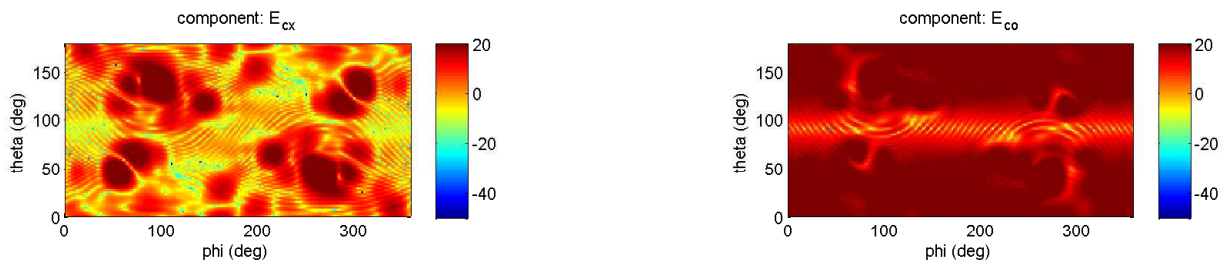
Figure 4.9: PO components
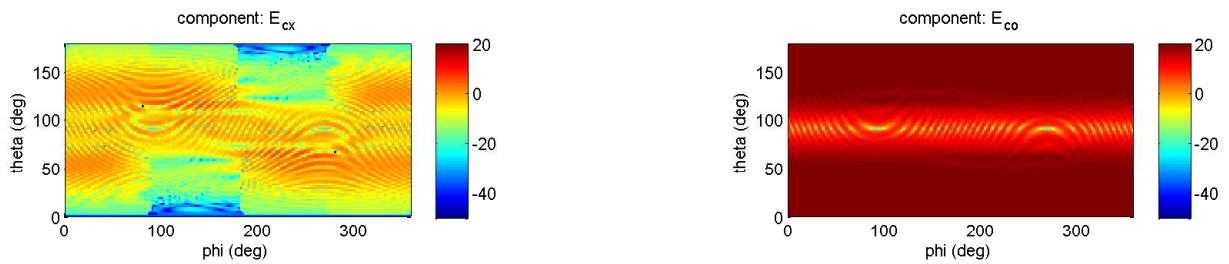
Figure 4.10: GTD components

63
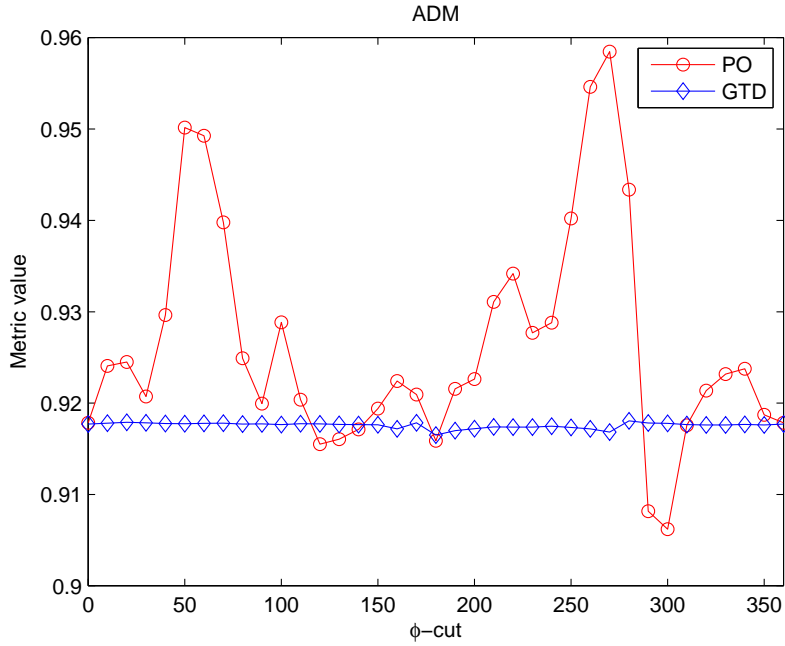
Figure 4.11: ADM Trend comparison

4.3.2 Metric trend evaluation

Assuming MOM model as reference field, we compute metrics relative to
Metric Set 1 for both PO and GTD modelling. We calculate metric values
on varying ϕ-cut, and we plot the trend of ADM, FDM and GDM for both
Single and Combined Antennapattern for TestCase1 and TestCase2.

	Test Case
Case 1	MOM vs. PO
Case 2	MOM vs. GTD

Table 4.3: Test cases

SingleAntennaPattern

In Figure (4.11), (4.12) and (4.13), trends of ADM, FDM and GDM for
SingleAntennaPattern are shown. Comparing the trend of metrics in the
two cases under discussion, it appears evident that metric values related to
TestCase1 are subject to substantial variations while moving from one cut to
another, whereas those related to TestCase2 are kept on the same level. We
can conclude that the considered configuration results to be a more critical
set-up for PO model validation with respect to GTD model.
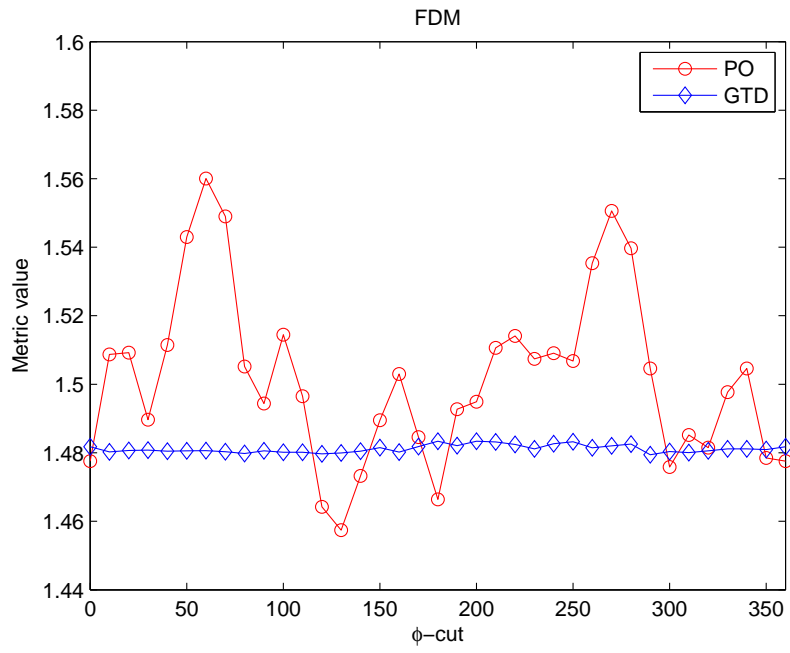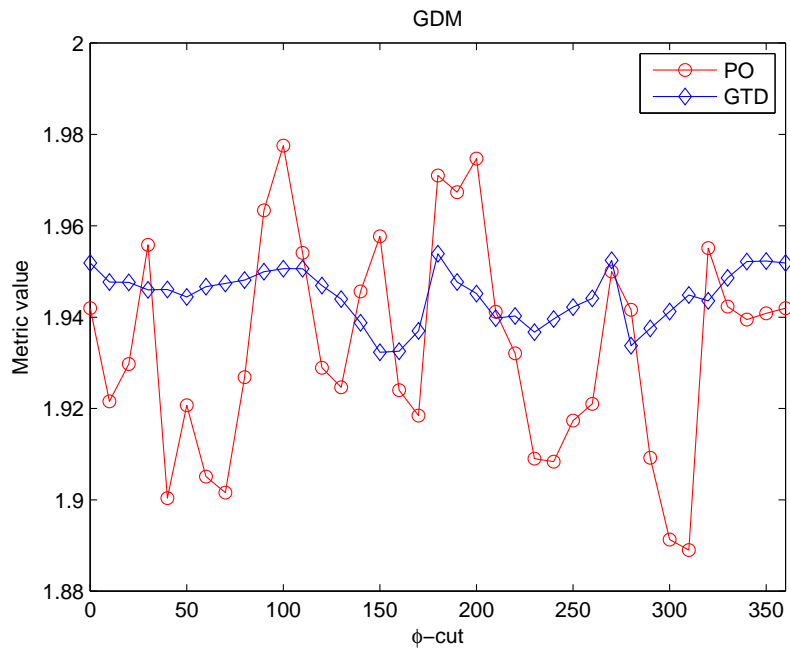
Figure 4.12: FDM Trend comparison
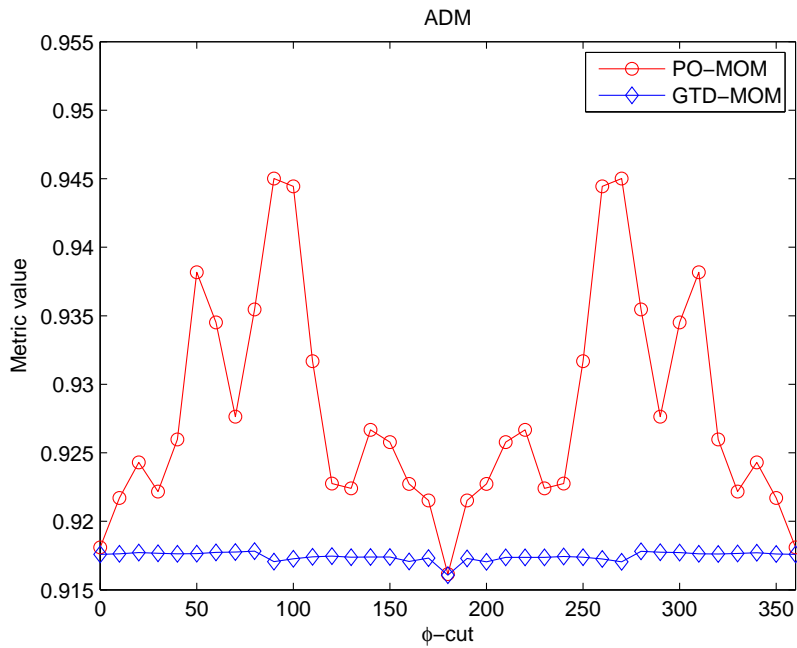

Figure 4.13: GDM Trend comparison

Figure 4.14: ADM Trend comparison

CombinedAntennaPattern

Similarly to the previously considered case, pattern trends of ADM, FDM and GDM for CombinedAntennaPattern are shown in Figure (4.14), (4.15) and (4.16). Comparing the trend of metrics in the two cases under discussion, it appears evident that metric values related to TestCase1 are subject to substantial variations while moving from one cut to another, whereas those related to TestCase2 are kept on the same level. We can conclude that the configuration with two antennas installed on opposite vertex of the cube results to be a more critical set-up for PO model validation with respect to GTD model.
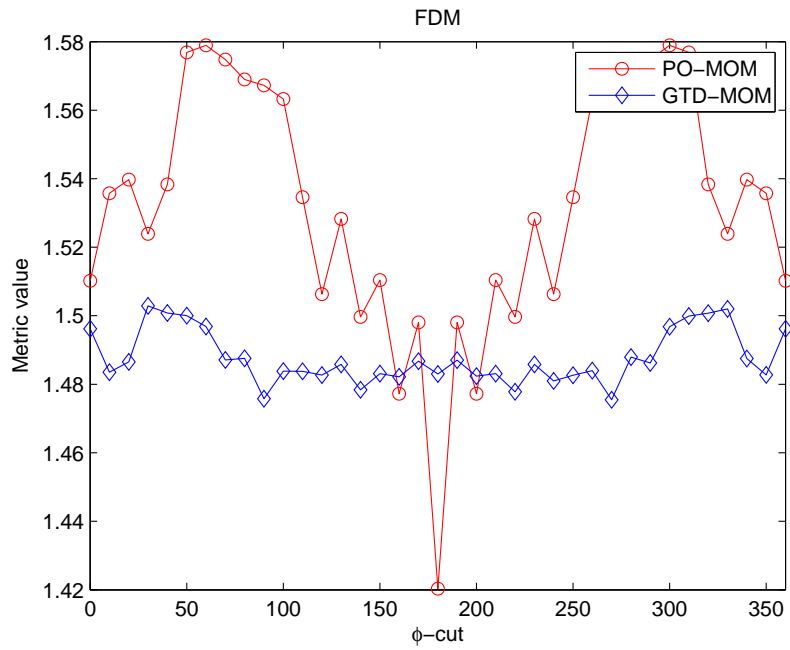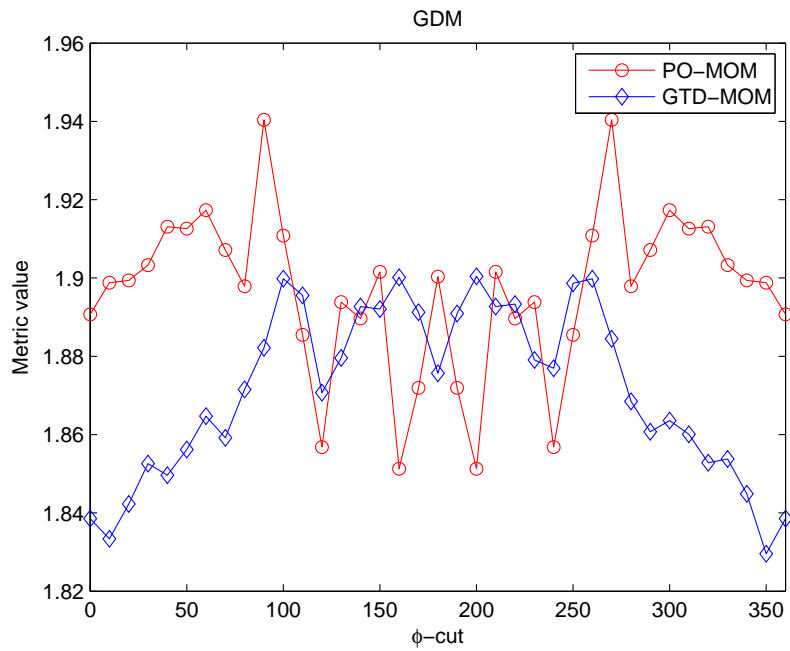
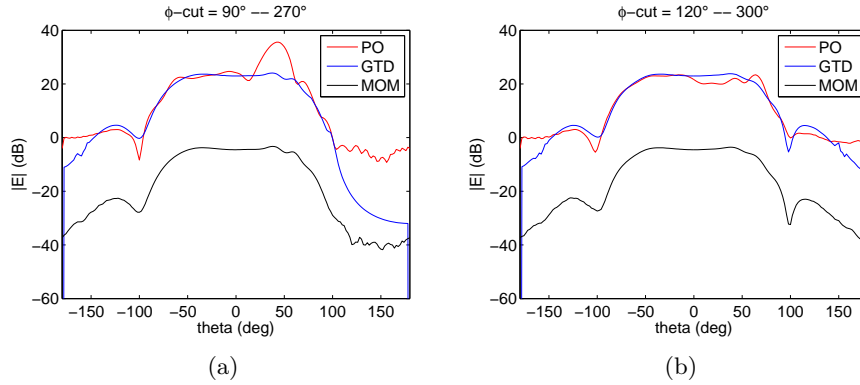Figure 4.15: FDM Trend comparison

Figure 4.16: GDM Trend comparison

Figure 4.17: Field SingleAntennaInstalled - relevant ϕ-cuts

4.3.3 Pattern comparison

Observing metrics trends computed in Section (4.3.2), we are interested in discovering and studying which ϕ-cut is responsible for the maximum variation of the slowly (ADM) or rapidly (FDM) changing features of the field, and which one for the minumum.

SingleAntennaPattern

Refer to Figure (4.11), the maximum amplitude in ADM corresponds to a region (ϕ-cut = 270) in which it is present a shading effect caused by the cube that generates ripples on the field for some portions of the sphere. The pattern relative to this cut is shown in Figure (4.17(a)). On the other side, pattern relative to the minimum amplitude in metric trend (ϕ-cut = 300) corresponds to a portion of the sphere out of the shaded region, and is shown in Figure (4.17(b)).

ϕ-cut	$270°$	$300°$
ADM value	0.958	0.905

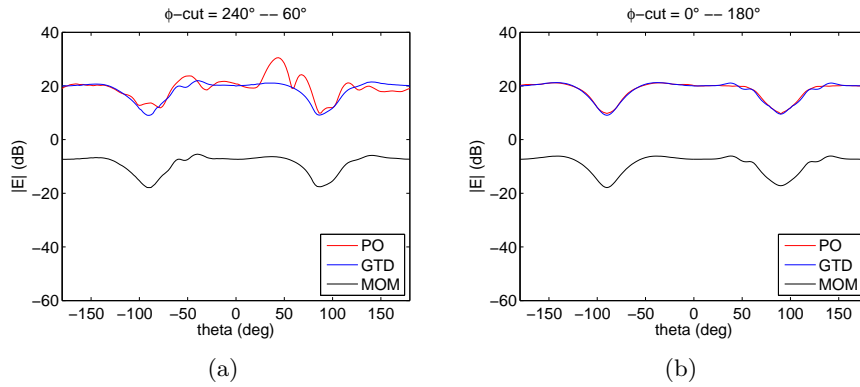Table 4.4: Metric value for relevant ϕ-cuts

68

Figure 4.18: Field CombinedAntennaPattern - relevant ϕ-cuts

CombinedAntennaPattern

Refer to Figure (4.15), the maximum amplitude in FDM corresponds to a region (ϕ-cut = 60) in which it is present a shading effect caused by the cube that generates ripples on the field for some portions of the sphere. The pattern relative to this cut is shown in Figure (4.18(a)). On the other side, pattern relative to the minimum amplitude in metric trend (ϕ-cut = 180) corresponds to a portion of the sphere in between the shade regions of the two installed antennas, and is shown in Figure (4.18(b)).

ϕ-cut	60°	180°
FDM value	1.579	1.420

Table 4.5: Metric value for relevant ϕ-cuts

69

4.4 Inter-pattern Analysis

A test we can do in order to investigate which radiation pattern among SingleAntennaPattern and CombinedAntennaPattern could be better for the validation of a model, in terms of error response, is to compare metric trends related to the same technique for different patterns. For this study FDM metric resulted to be a case of particular interest. Consider GTD modelling, in Figure (4.19) are shown normalized components that measure the rapidly changing features for CombinedAntennaPattern and SingleAntennaPattern. In the first case, the metric trend on varying ϕ-cut has stronger fluctuations with respect to the latter, and so the first pattern is more sensitive to errors introduced by this techique. We can conclude that in order to validate a simulation based on GTD modelling, a configuration with two antennas installed on a cube would be preferable with respect to a configuration with only one. In order to verify and quantify what observed, we compute for both Single and Combined AntennaPattern the maximum and the minimum percent variation of the metric value for a ϕ-cut from the mean value on the full sphere. Results are shown in Tab.(4.6). Observing the last column of the table, we can notice that the variations related to the second pattern under analysis are several times larger than those related to the first one.

	SingleAntennaPattern	CombinedAntennaPattern	% var. ratio
(max % var.)	0.15%	1.02%	6.8
(min % var.)	-0.11%	-0.82%	7.5

Table 4.6: GTD simulation

On the other hand, this analysis can not lead us to similar clear conclusions for PO modelling. In fact, as shown in Figure (4.20) with corresponding data reported in Tab.(4.7), metrics computed for the two cases have similar trends, and this study does not provide us additional information to decide in favour of a pattern or the other one.

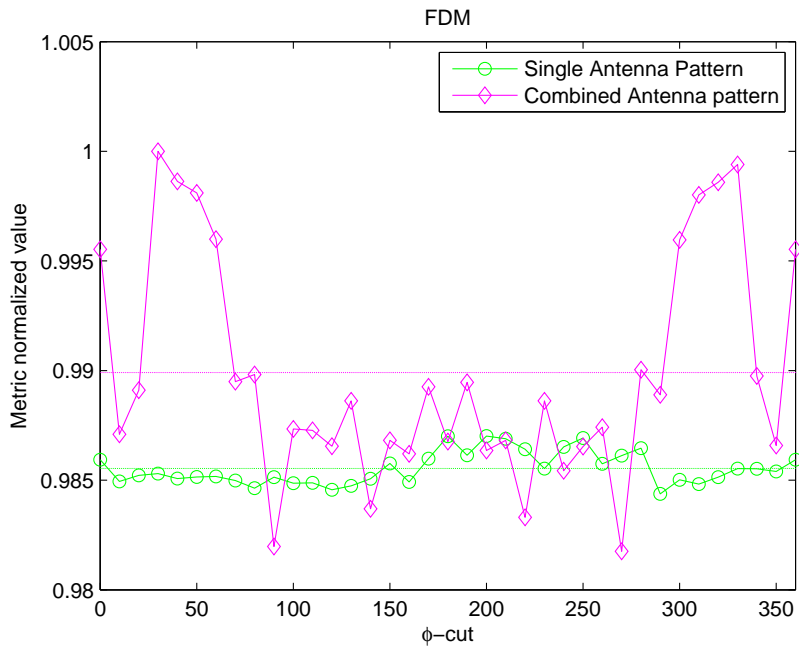|	SingleAntennaPattern	CombinedAntennaPattern	% var. ratio
(max % var.)	3.88%	3.06%	0.78
(min % var.)	-2.95%	-7.30%	2.47

Table 4.7: PO simulation

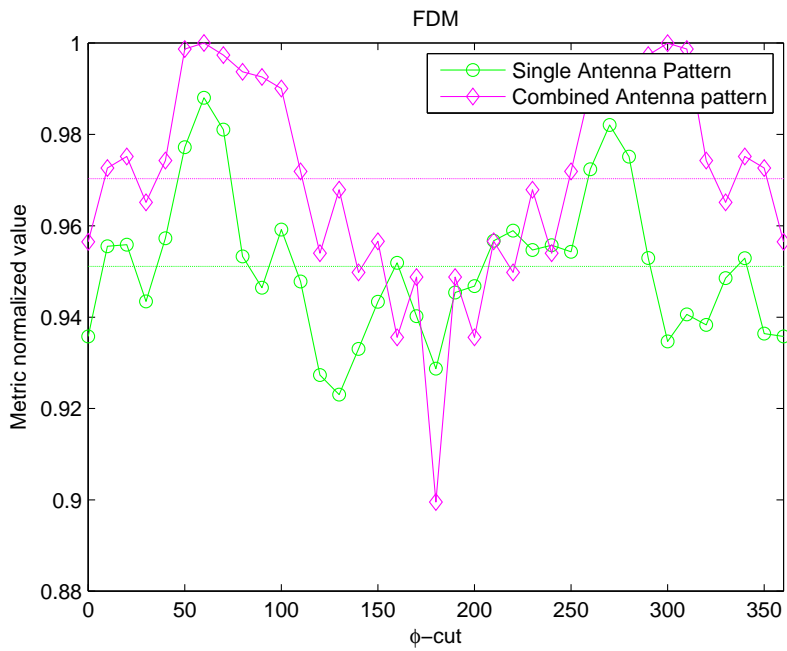Figure 4.19: GTD modelling - FDM trend comparison

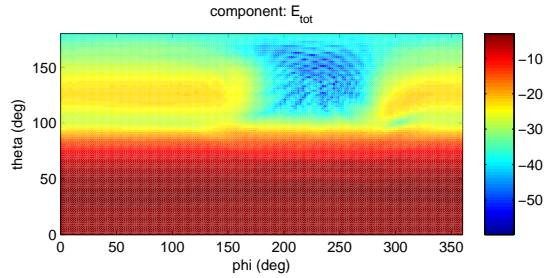Figure 4.20: PO modelling - FDM trend comparison

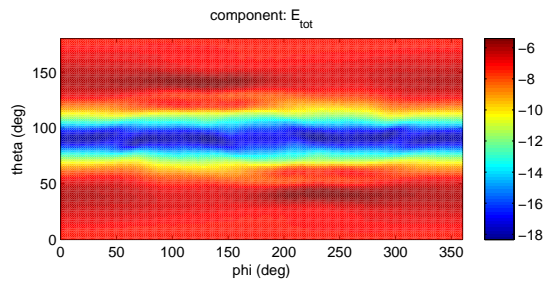Figure 4.21: Reference SingleAntennaPattern - (MOM)

Figure 4.22: Reference CombinedAntennaPattern - (MOM)

4.5 Validation - Evaluation procedure

So far, we have been considering test cases in which one or more given patterns were discussed in order to define a set of reference critical configurations in preparation of a validation procedure. After selecting the validation reference, a method of evaluating that reference must be employed. The Feature Selective Validation (FSV) procedure combined with metrics introduced in Section (2.5) is used to determine if the agreement between the validation reference and the new simulation results is acceptable.

We are now interested in showing how a validation procedure actually works, assuming MOM simulated pattern as reference, and PO-GTD models as those to be validated. First, we analyze the SingleAntennaPattern configuration, and second, the CombinedAntennaPattern.

Test cases we are interested in studying are reported in Tab.(4.8).

	Test Case
Case 1	MOM vs. PO
Case 2	MOM vs. GTD

Table 4.8: Test cases

72

4.5.1 SingleAntennaPattern

Field simulation

Pattern simulations provided by software modelling tool for PO and GTD techniques are reported in Figure (4.23), (4.24). Reference pattern is shown in Figure (4.21).
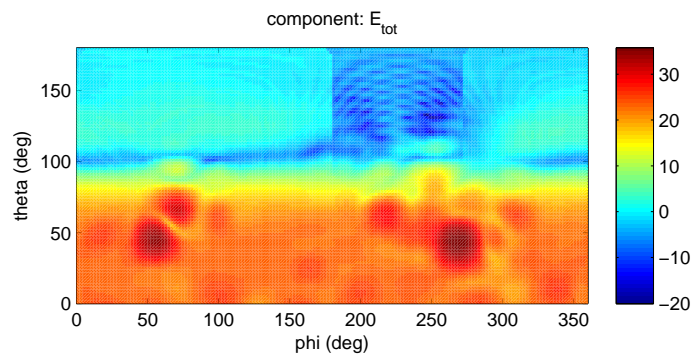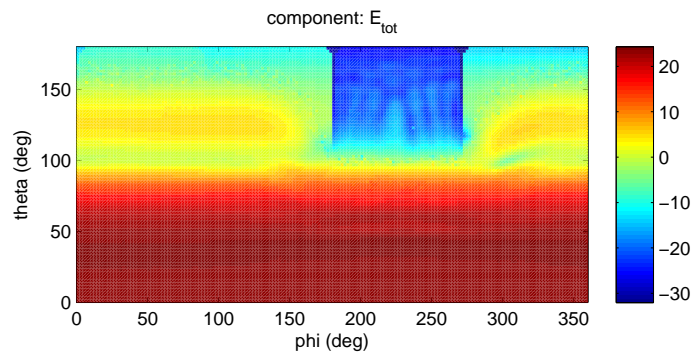

Figure 4.23: PO simulated antenna pattern

Figure 4.24: GTD simulated antenna pattern
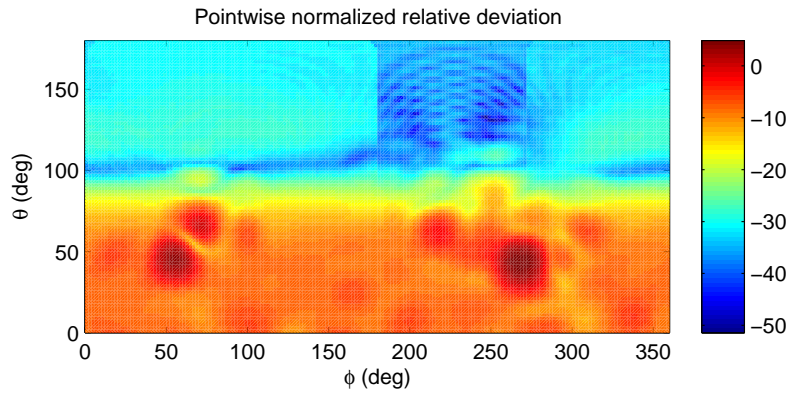
Metrics evaluation - Case 1

Figure 4.25: SingleAntennaPattern MOM vs. PO - Relative Deviation

Metric Set 1	Value	Evaluation
ADM	0.926	Poor
FDM	1.502	Poor
GDM	1.922	Very Poor

Table 4.9: Case 1: MOM vs. PO

Metric Set 2	Value
Field Relative Residual	29.62 dB
Degree of correlation	0.83

Table 4.10: Case 1: MOM vs. PO

Metrics evaluation - Case 2

Pointwise normalized relative deviation
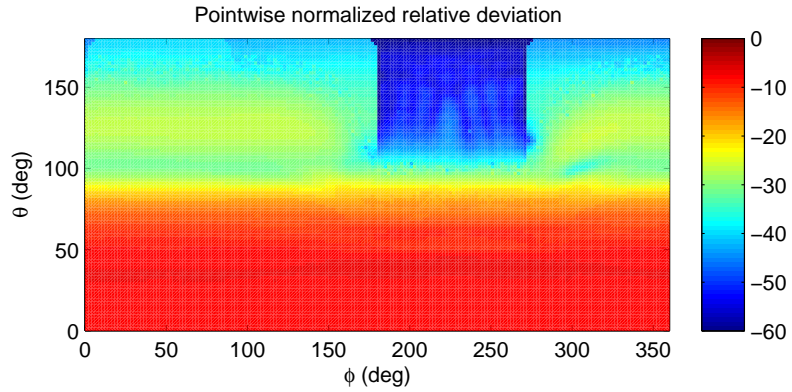
Figure 4.26: SingleAntennaPattern MOM vs. GTD - Relative Deviation

Metric Set 1	Value	Evaluation
ADM	0.917	Poor
FDM	1.480	Poor
GDM	1.910	Very Poor

Table 4.11: Case 2: MOM vs. GTD

Metric Set 2	Value
Field Relative Residual	26.95 dB
Degree of correlation	0.98

Table 4.12: Case 2: MOM vs. GTD

4.5.2 CombinedAntennaPattern

Field simulation

Pattern simulations provided by software modelling tool for PO and GTD techniques are reported in Figure (4.27), (4.28). Reference pattern is shown in Figure (4.22).
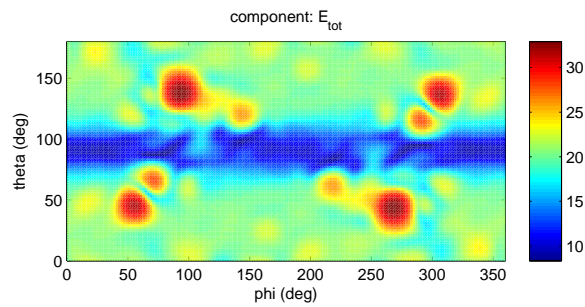

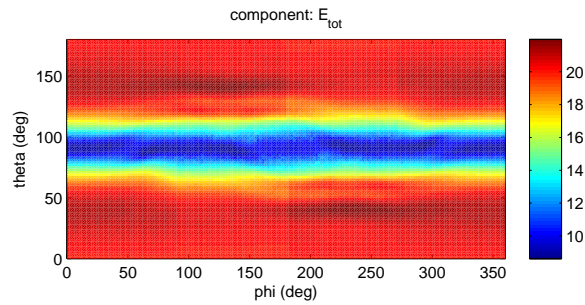Figure 4.27: PO simulated antenna pattern

Figure 4.28: GTD simulated antenna pattern
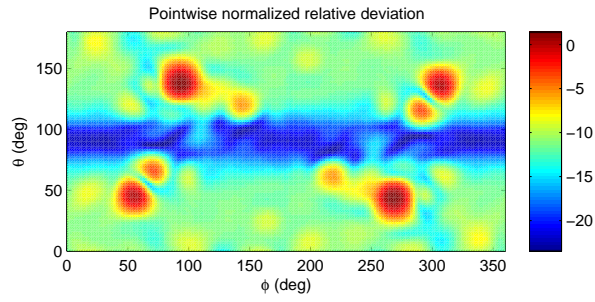
Metrics evaluation - Case 1

Pointwise normalized relative deviation

Figure 4.29: CombinedAntennaPattern MOM vs. PO

Metric Set 1	Value	Evaluation
ADM	0.931	Poor
FDM	1.510	Poor
GDM	1.922	Very Poor

Table 4.13: Case 1: MOM vs. PO

Metric Set 2	Value
Field Relative Residual	29.47 dB
Degree of correlation	0.85

Table 4.14: Case 1: MOM vs. PO

Metrics evaluation - Case 2
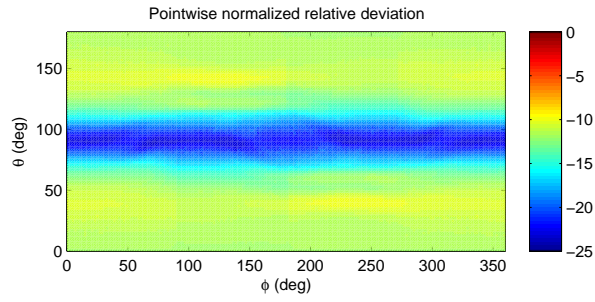
Figure 4.30: CombinedAntennaPattern MOM vs. GTD

Metric Set 1	Value	Evaluation
ADM	0.916	Poor
FDM	1.485	Poor
GDM	1.916	Very Poor

Table 4.15: Case 2: MOM vs. GTD

Metric Set 2	Value
Field Relative Residual	26.93 dB
Degree of correlation	0.98

Table 4.16: Case 2: MOM vs. GTD

4.5.3 Results analysis

Referring to data reported in tables and figures of Section (4.5), we can notice that for both patterns under discussion, metric values related to GTD are slightly better if compared to those related to PO, but remain far away from giving results that can make us consider PO and GTD modelling as accurate. Anyway, the focus of this analysis was not on the result itself but on the methodology that had to be followed in order to give a quantitative indication of the accuracy of a simulation with respect to a reference model, that is the core of a validation procedure.

Chapter 5

Satellite-Antennas configurations

Different antennas have been selected to be installed on the satellite mock-up in order to collect data for the validation procedure. As stated in the previous chapters, we are interested in measurement configurations that can stress the weakness of the CEM model. All the antennas will be installed on the top panel of the platform, that in a real telecommunications satellite is pointed towards the ground. Once decided for antennas to use, we designed and fabricated aluminum supports in order to physically interface antennas with the satellite.
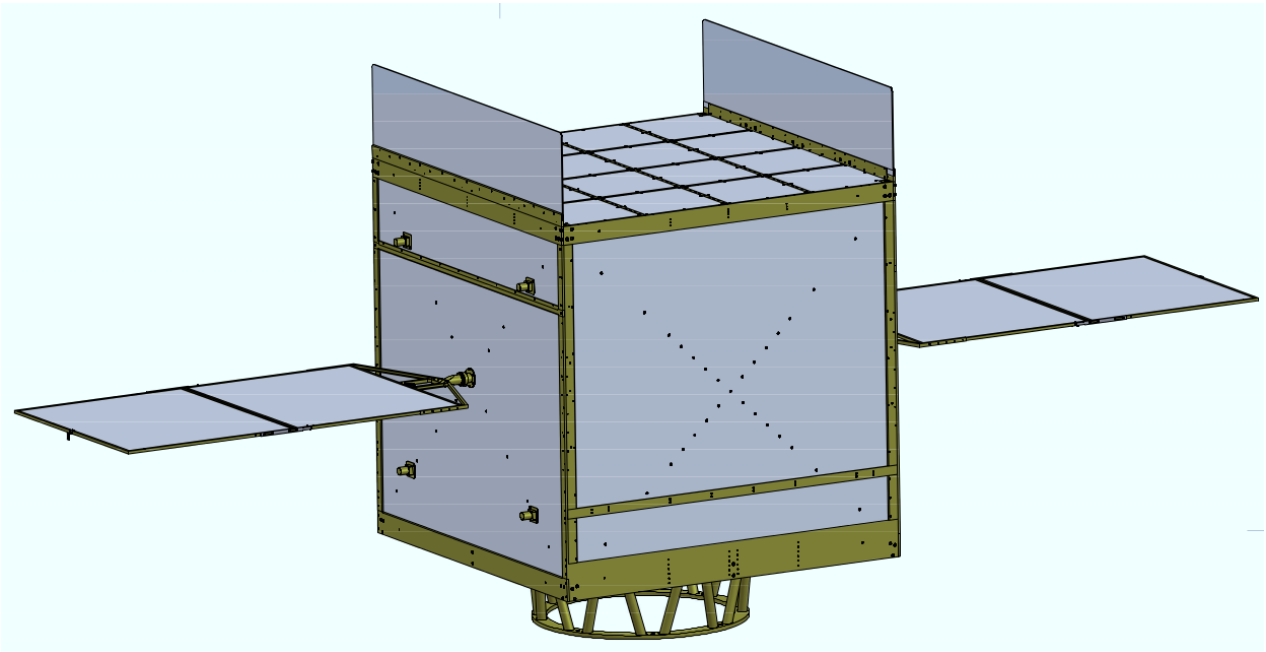

Figure 5.1: FUSS satellite model

5.1 Reflector Antenna

The first antenna we consider is a Ku-band reflector antenna, a spare of the TVB3 antenna (TV Broadcast 3) installed on Olympus, a sperimental satellite for telecommunications launched by ESA the 12th of July 1989; a picture is shown in Fig.(5.2).

Figure 5.2: Reflector Antenna with interfacing support

This antenna is capable of interfacing the satellite in two different configurations; see Fig.(5.3) and (5.4). Red circles highlight the considered interfacing configuration.

The reflector and the feed will be fixed on an aluminum, 4mm-thick, mounting support, ready to be installed on the mock-up according to the previously mentioned configurations. Furthermore, we designed a second aluminum support, 10mm-thick, in order to perform measurements of the antenna alone; see Figure (5.5) Infact, the latter will be capable of interfacing the first support-antenna structure with the positioning device of the anechoic chamber.

Typically, antennas involved in a validation campaign are no longer in use antennas. Therefore, the preparation phase has to include the understanding of the original configuration of the antennas. In particular, for the reflector antenna, the reconstruction resulted to be very struggling, as geometrical data necessary to complete the knowledge of the feed-reflector geometry and design a proper model were missing.
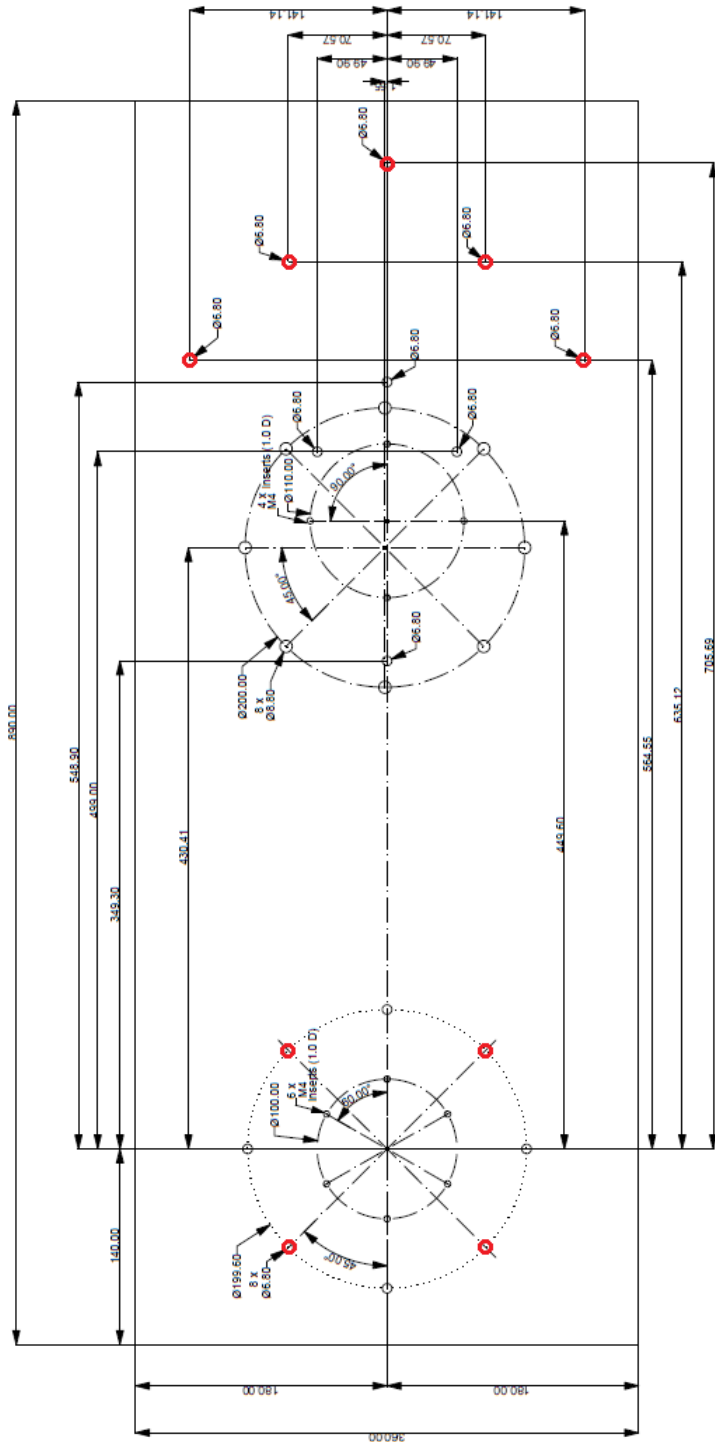
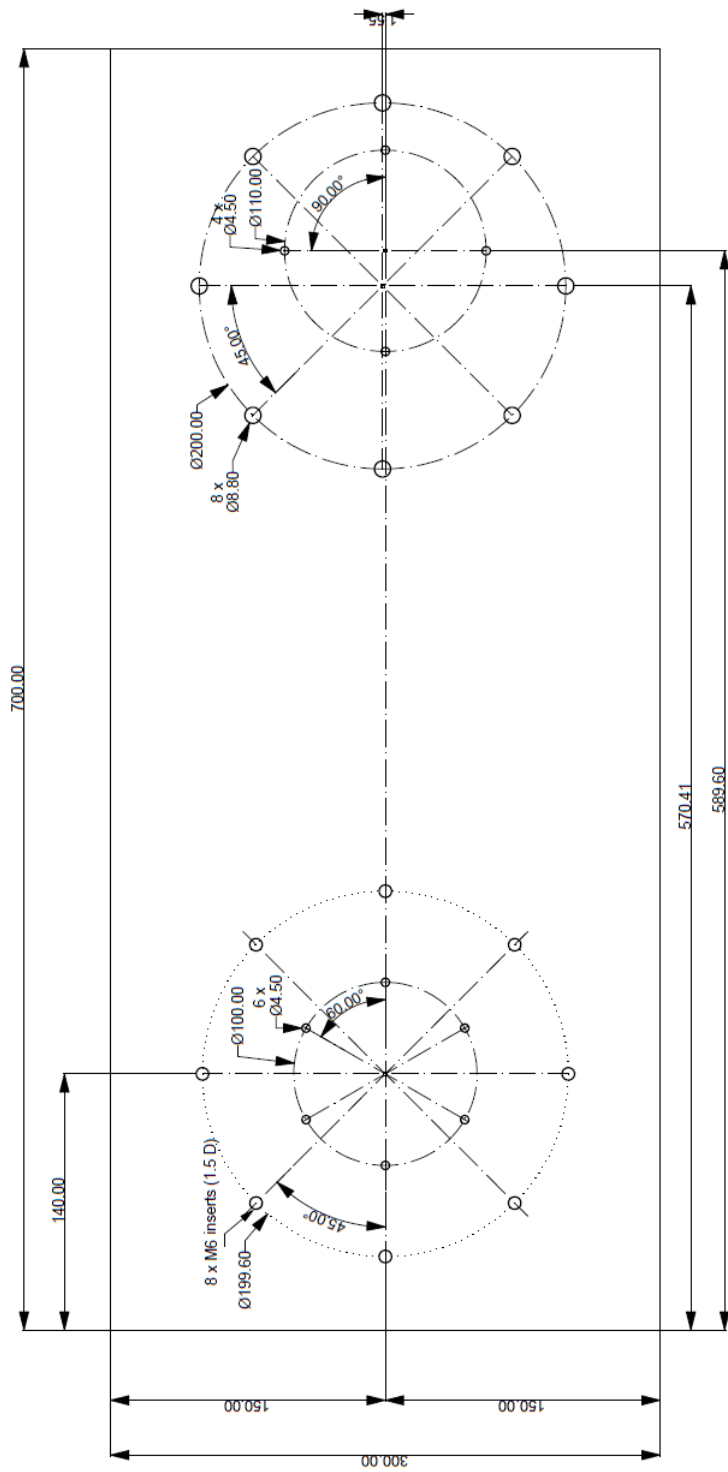Figure 5.3: Reflector Antenna 4mm interfacing support - Configuration 1

Figure 5.4: Reflector Antenna 4mm interfacing support - Configuration 2

Figure 5.5: Reflector Antenna 10mm interfacing support

5.2   Feed Antenna

The second antenna is a Ku-band feed, a picture is shown in Fig.(5.6). This antenna can provide a relevant test case if considered indipendently. Furthermore, it is fundamental to obtain the radiation pattern of the reflector antenna feed, as it is frequently responsible for a direct radiation of the satellite itself.
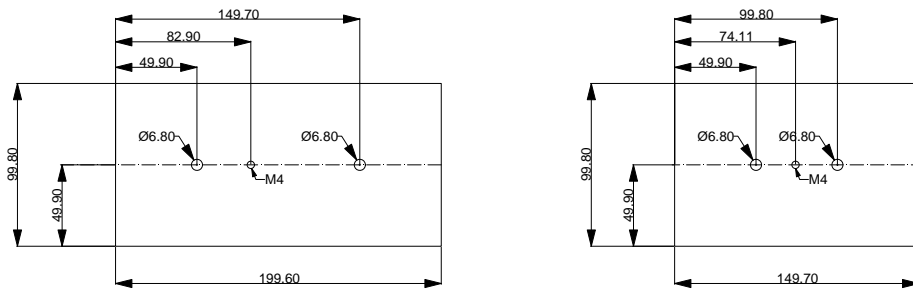

Figure 5.6: Feed Antenna

Figure 5.7: Antenna 2 support

5.3   Array Antenna

The third antenna is an L-band array antenna. This antenna can interface the satellite using a 3-support structure as in Figure (5.7).

5.4   Metasurface Antenna

The last antenna under test is an X-band Metasurface HGA; a picture is shown in Fig.(5.8).
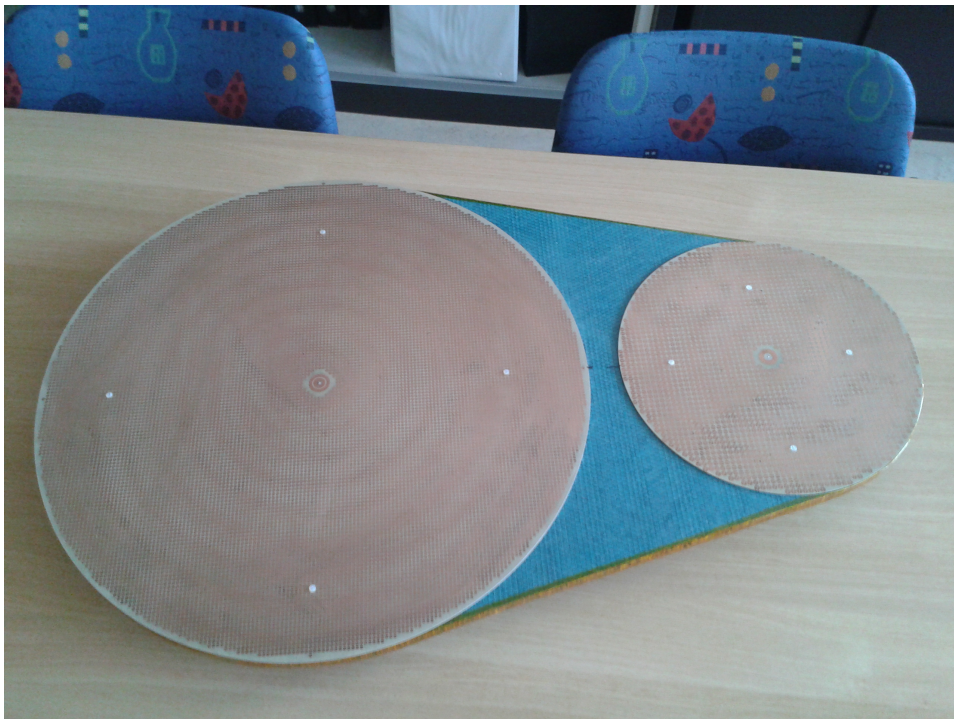

Figure 5.8: Metasurface Antenna

Conclusion

The thesis work concerned the analysis and the validation of computational electromagnetic modelling techniques applied to space antenna modelling. We developed a simple error model suitable to emulate their basic behaviour. The model assumed a constant absolute numerical error introduced over the pattern for PO modelling, and a constant relative numerical error for GTD/UTD modelling.

Errors were applied to a number of test cases; simple antennas radiation patterns were simulated via MATLAB, whereas configurations involving a cubical supporting structure required a more sophisticated software tool. Some sets of indicators, referred to as metrics, helped us in evaluating the departure from a reference behaviour. A number of specialized procedures were developed in order to identify the best suited cases to classify hardware test configurations for validation purposes. The "intra-metric" study allowed to decide among a set of patterns those that can result critical for the validation of a model with a given underlying CEM technique. On the other side, the "intra-pattern" study allowed, for a given reference pattern, to decide among various CEM techniques for the one that results to be particulary stressed in simulating that field.

As a result of this process, we designed and built a number of mechanical interfaces to adapt antenna hardware to a satellite mock-up to actually perform the desired tests.

Bibliography

[1] Giordanengo G., Sabbadini M., *Fast Antenna Testing With Reduced Near Field Sampling*, IEEE Transactions on Antennas and Propagation, vol. 62, no. 5, May 2014, pp. 2504-2506.

[2] IEEE Electromagnetic Compatibility Society, *IEEE Standard for Validation of Computational Electromagnetics Computer Modeling and Simulations*, IEEE, 2008.

[3] Keller, J.B., *The geometric optics theory of diffraction*, presented at the 1953 McGill Symp. Microwave Optics, A.F. Cambridge Res. Cent., Rep. TR-59-118 (II), pp. 207-210. 1959.

[4] Kouyoumjian, R. G. and Pathak, P. H., *A uniform geometrical theory of diffraction for an edge in a perfectly conducting surface*, Proc. IEEE, vol. 62, pp. 1448–1461, November 1974.

[5] McNamara, D. A., *Introduction to the Uniform Geometrical Theory of Diffraction*, Boston, MA: Artech House, 1990.

[6] Milligan, T.A., *Modern Antenna Design*, Hoboken, Wiley, 2005, 2nd edition.

[7] Sarkar, T. K., *Method of Moments Applied to Antennas*, Syracuse University, N.Y., 2000.

[8] Struik, D.J., *Differential Geometry* Addison-Wesley, Reading, MA, 1950, p.55.

[9] Tancioni L., Spherical Wave Expansion, ESA Document, February 2011, pp.7-26.